



# Designing Twisted Bilayer Graphene Based Devices

*Thesis submitted in partial fulfilment of the  
requirements for the degree  
of*

**Masters in Science (M.Sc.)**

*by*

**Jovi K**

P0181214

UM DAE CEBS

*Under the guidance*

*of*

**Dr. Romain Danneau**

Institut für Nanotechnologie

Karlsruher Institut für Technologie



## Certificate

This is to certify that CEBS student Mr. JOVI K, P0181214 has undertaken project work from 01 July 2022 to 31 Dec 2022 under the guidance of Dr. ROMAIN DANNEAU, Institut für Nanotechnologie, Karlsruher Institut für Technologie.

This submitted project report titled DESIGNING TWISTED BILAYER GRAPHENE BASED DEVICES is towards the academic requirements of the M.Sc. Thesis Project Course at UM-DAE CEBS, Mumbai.

Jovi K

Name & Signature of Student with Date

Dr. Romain Danneau

Name & Signature of Advisor(s) with Date

## Acknowledgement

I would like to extend my appreciation to those who have contributed to the successful completion of this project with their dedication and patience.

I am deeply grateful to my supervisor, Dr. Romain Dannean, for introducing me to this fascinating subject and for serving as a constant source of inspiration. With a hands-on approach to advising, Dr. Dannean provided me with a significant degree of intellectual and creative freedom in designing my own experiments and was always available to offer guidance and direction. The interactive nature of our relationship has greatly enhanced my problem-solving abilities, a skill that I will treasure forever. His guidance was invaluable throughout the duration of my project and in the writing of this report.

I am also grateful to Prof. Ralph Krupke for providing me with the opportunity to join the research group and for ensuring a smooth transition into the team.

I would like to express my sincere appreciation to my fellow group members, particularly Devang and Paul, for sharing their expertise on stacking and for their invaluable suggestions throughout my time in the group. Their willingness to challenge me and provide constructive feedback has been invaluable to my growth as a researcher. I wish them the best in all their future endeavors.

I also want to thank Simone for her patience and thorough training in fabrication techniques.

Lastly, I am grateful to my family and friends for their unwavering support and encouragement. Special thanks to my parents for their love and for pushing me to be the best version of myself. Despite being twelve time zones away, they never failed to provide the mental and financial support that was crucial to the completion of this thesis.

I would also like to acknowledge those who have contributed to the manuscript by carefully reviewing an early draft and providing valuable comments and suggestions that have been incorporated to improve the presentation.

## Abstract

The investigation of the characteristics of van der Waals heterostructures is a rapidly growing area of research in condensed matter physics, with significant potential but still in its infancy. Graphene, known as a "wonder material" due to its exceptional properties such as superior electrical conductivity compared to copper and strength 200 times that of steel, had yet to exhibit the quantum phenomenon of superconductivity. However, in 2018, a remarkable discovery revealed that superconductivity could be achieved in Twisted Bilayer Graphene, a structure consisting of two layers of graphene placed on top of each other with a rotation angle near the "Magic Angle" of 1.1 degrees. These findings and many others have spurred a surge of research in the field of twistrionics in experimental condensed matter physics, leading to the need for optimization and standardization of fabrication procedures for reproducibility and improve the quality of stacks. In this thesis, we aim to standardize the method of fabricating twisted Bilayer Graphene using the modified Dry Stacking Method and the recent technique of tear and stack procedure. We conclude with the successful implementation of a standardized step-by-step procedure for a typical TBLG stack.

# Table of Contents

Designing Twisted Bilayer Graphene Based Devices .....	1
Abstract .....	2
Acknowledgement .....	3
1. Introduction .....	7
1.1 The world of 2D materials .....	8
1.2 Van der Waals Heterostructures .....	8
1.2.1 Twistronics .....	9
1.3 Objectives .....	10
1.4 Thesis Outline .....	10
2. Physics of graphene-based structures .....	11
2.1 Band structure of SLG .....	11
2.1.1 Energy bands .....	13
2.2 Bilayer Graphene .....	15
2.2.1 Band Structure for Bernard Stacking .....	17
2.2.2 Periodic potentials in twisted bilayer graphene .....	18
2.3 Correlated Insulators and Superconductivity in Magic Angle Twisted Bilayer Graphene .....	22
3. Experimental Fabrication Procedure .....	24
3.1 Mechanical exfoliation .....	24
3.2 Characterisation of 2D crystallites .....	25
3.2.1 Raman Spectrum of Graphene .....	26
3.2.2 AFM on hBN .....	28
3.3 vdW heterostructure assembly .....	28
3.3.1 hBN encapsulation .....	28
3.3.2 Dry stacking Technique .....	29
3.3.3 Dropping the stack from stamp .....	30
4. Modified Dry Stacking Procedure for tBLG .....	31
4.1 Challenges for fabricating tBLG .....	33
4.2 Tear Problem .....	33

4.2.1	Tear using hBN flake.....	35
4.2.2	Tear using AFM Tip.....	35
<b>4.3</b>	<b>Clean Interface Problem.....</b>	<b>36</b>
4.3.1	Rectangular Stamp .....	37
4.3.2	Convexo-Rectangular Stamp .....	39
<b>4.4</b>	<b>Spectrum of Large angle tBLG.....</b>	<b>40</b>
<b>4.5</b>	<b>Post Cleaning Processes.....</b>	<b>41</b>
<b>4.6</b>	<b>Results.....</b>	<b>42</b>
<b>4.7</b>	<b>Future Prospects .....</b>	<b>46</b>
<b>5.</b>	<b>References.....</b>	<b>47</b>

(This page intentionally left blank)

# 1. Introduction

God made the bulk; the surface was invented by the devil.

---

Wolfgang Pauli

It is now well known that the surface phenomenon can be drastically different from the bulk and Surface Science is one of the main research fields in Condensed Matter Physics. Physicists have always been on the lookout for ways to separate the bulk from the surface<sup>1</sup>. The exfoliation of graphene [1], a 2D 1-atom thick van der Waal material generated a tremendous amount of interest for its promising physical and electronic properties.

Two-dimensional (2D) crystals are recent examples of promising new materials, graphene being just the most known example of this large class. Having as principal feature their low dimensionality, these 2D crystals present unique physical properties that already have many technological applications. The continuous refinement and optimization of their manufacturing processes and decreasing production costs are responsible for an increasing impact in industry and are expected to lead these crystals to be more and more present in our lives.

Taking into account that the current fabrication methods of 2D crystals are sufficiently well established (at least for some of them), a new trend in modern materials science is to develop novel three-dimensional (3D) materials by controlled multi-stacking of these 2D structures. The variety of possible heterostructures generated, often referred to as van der Waals (vdW), seems to be practically unlimited but, at the same time, their behaviour is expected to be hard to predict due to the huge complexity of each 2D structure involved. Why consider stack of different materials, a bilayer stack made of same material but with a twist gave rise to a whole new field of Twistronics.

In this thesis, we focus on one of the simplest stackings, the twisted bilayer graphene (tBLG) —a graphene sheet on top of other graphene sheet, with a twist angle and aims to create a standard procedure for fabrication of these stacks. Recent discovery of Mott insulation and Superconductivity in tBLG has received tremendous attention and optimising the fabrication of these devices is very crucial in further exploring the mysteries it beholds.

---

<sup>1</sup> A surface is of fundamental importance in physics not only because of the abrupt change in the boundary conditions, but also as, it is when one dimension becomes comparable to the electron wavelength and quantum effects starts to dominate.

Graphene family	Graphene	hBN 'white graphene'	BCN	Fluorographene	Graphene oxide
2D chalcogenides	MoS <sub>2</sub> , WS <sub>2</sub> , MoSe <sub>2</sub> , WSe <sub>2</sub>		Semiconducting dichalcogenides: MoTe <sub>2</sub> , WTe <sub>2</sub> , ZrS <sub>2</sub> , ZrSe <sub>2</sub> and so on	Metallic dichalcogenides: NbSe <sub>2</sub> , NbS <sub>2</sub> , TaS <sub>2</sub> , TiS <sub>2</sub> , NiSe <sub>2</sub> and so on	
				Layered semiconductors: GaSe, GaTe, InSe, Bi <sub>2</sub> Se <sub>3</sub> and so on	
2D oxides	Micas, BSCCO	MoO <sub>3</sub> , WO <sub>3</sub>	Perovskite-type: LaNb <sub>2</sub> O <sub>7</sub> , (Ca,Sr) <sub>2</sub> Nb <sub>3</sub> O <sub>10</sub> , Bi <sub>4</sub> Ti <sub>3</sub> O <sub>12</sub> , Ca <sub>2</sub> Ta <sub>2</sub> TiO <sub>10</sub> and so on		Hydroxides: Ni(OH) <sub>2</sub> , Eu(OH) <sub>2</sub> and so on
	Layered Cu oxides	TiO <sub>2</sub> , MnO <sub>2</sub> , V <sub>2</sub> O <sub>5</sub> , TaO <sub>3</sub> , RuO <sub>2</sub> and so on			Others

Figure 1.1: Current 2D library: Monolayers that has been shown to be stable in ambient conditions is shaded blue; monolayers that is likely stable is shaded green; monolayer that is unstable in air but might be stable in an inert atmosphere is shaded pink. Indicated by grey shading are 3D compounds that have effectively exfoliated to monolayers but for which little additional information is available. [35]

## 1.1 The world of 2D materials

Nowadays, there is a vast library of existent 2D crystals (Fig. 1.1). Amongst them, graphene is an unequivocal champion, exhibiting outstanding properties that have attracted widespread interest from the scientific community all over the world. A brief insight of some of those properties which have triggered so much attention in a wide variety of scientific areas:

Graphene has very high tensile strength [2] of 130 GPa and Young's Modulus of 1TPa (strongest material currently known) and exceptionally high thermal conductivity [3,4] ideal for, say, heat dissipation in integrated circuit-based electronic systems.

Beside its materials peculiarities, physicists were fascinated by the electronic properties of graphene due to its "massless" charge carriers which show gapless energy dispersion whose density of states vanishes linearly when approaching the Fermi energy. Graphene can be considered a "bridge material" between metals and semiconductors' world, what is called a "Semi-metal" [5]. Notable observations in the quantum regime include quantum hall effect at room temperature [6] and Bipolar Supercurrent [7] to name a few.

## 1.2 Van der Waals Heterostructures

Another research area has recently evolved in parallel with the work being done on graphene and other 2D materials; it deals with vdW heterostructures, artificial structures produced by piling 2D crystals on top of one another (Fig. 1.2). The basic idea is straightforward: we build artificial materials out of blocks defined with one-atomic plane precision by stacking monolayers in a predetermined order, much like when building with Legos. Strong covalent bonds provide the in-plane stability of 2D

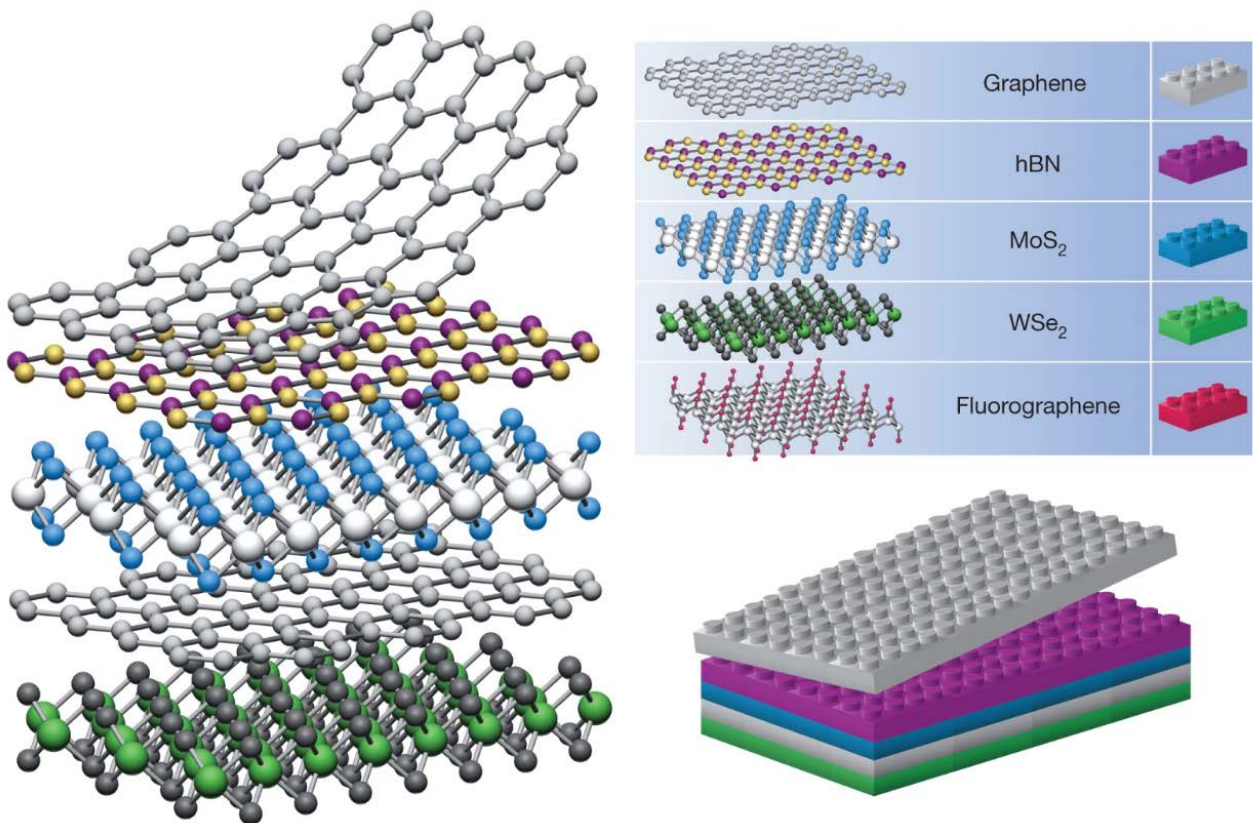


Figure 1.2: In the world of Lego Physics [35]

crystals, while relatively weak van der Waals like forces should be enough to keep the stack together. Van der Waals (vdW) materials are a subclass of materials that contain strong van der Waals forces between atoms in the same layer and weak van der Waals forces between atoms in different levels.

The goal is to create artificial heterostructures with tailored properties for technological applications using the existing variety of 2D materials, each of which exhibits distinct properties. The main benefit of this strategy is that it should be possible to create materials that can serve multiple purposes at once. Even though this discipline is still in its infancy, vdW heterostructures certainly have ambition. The flexibility offered in this context is immense. For example, it is very easy to integrate graphene (a semi metal) into a vdW heterostructure with a superconductor [8], semiconductors with strong spin-orbit coupling [9], quantum spin hall insulators [10], and ferromagnetic insulators [11].

### 1.2.1 Twistronics

In fact, this material is so versatile that, under the appropriate conditions, in the form of stacking the same 2-D material on top of each other with a small degree of rotation between the two layers (known as **twisting**) can give rise to a superconductor [12], an insulator [13] or a ferromagnet [14]!

The very idea of Twisted Bilayer Graphene (TBG) took the world of 2-D physics by storm and emergence of a new field known as **Twistronics**.

These and many more like orbital magnetism or Chern insulators can be achieved by tuning the Fermi level using an electrostatic gate. This was achieved by twisting two sheets of single-layer graphene on top of each other by approximately  $1.1^\circ$ , which is known as Magic Angle Twisted Bilayer Graphene (MATBG).

### 1.3 Objectives

These discoveries and a lot more theoretical predictions in tBLG would certainly mean that perfecting the manufacture of these devices is crucial to uncovering more of the mysteries it holds. The aim of this thesis is to design a **fabrication procedure for twisted bilayer graphene-based structures with controllable twist angles**, which has not previously been explored in our group.

Time constraints considering the technical complexity and the lack of a high precision rotation stage meant that fabricating and doing a full-fledged transport measurement on Magic Angle tBLG (at  $1.1^\circ$  twist angle) was impossible and the program was cut short to only the fabrication part.

### 1.4 Thesis Outline

The outline of this thesis report is as follows: Chapter 2 aims to update the reader with a theoretical background and predictions which effectively act as the motivation for fabrication of the tBLG, whereas Chapter 3 and 4 is more experiment oriented. Chapter 3 describes the fabrication process for heterostructures as done in the field and in our group, while Chapter 4 is modular and focuses on optimising the existing procedure to fabricate twisted Bilayers and essentially encompasses the work done during the thesis.

In Chapter 2, the focus is on providing the reader with a theoretical background and predictions that serve as motivation for the fabrication of twisted bilayer graphene (tBLG). This includes a discussion on the energy bands of Single Layer Graphene (SLG), Bernard Stacked BLG and the tBLG. The chapter aims to act as a motivation for fabrication of twisted BLG.

Chapters 3 and 4 shift the focus to the experimental aspect of the research. Chapter 3 describes the fabrication process for heterostructures, which is a common technique used in the field and in our research group. This includes a detailed explanation of the various steps involved, as well as the challenges that are faced during the fabrication process. In contrast, Chapter 4 focuses on optimizing the existing procedure for fabricating tBLG. This chapter highlights the specific work done during the thesis, including any innovations or modifications to the fabrication process that were developed. Overall, these two chapters provide a comprehensive understanding of the fabrication process and the progress made in the field.

## 2. Physics of graphene-based structures

What is important about graphene is the new physics it has delivered.

Andre Geim

In this chapter, we aim at deriving a model for the tBLG system. As starting point, we explain the tight-binding model for SLG, which allow us to introduce general concepts and fix notation. Within the SLG system, we also investigate the folded description, since it will provide us a better understanding of the tBLG system. Then, we move to the bilayers. We begin with a particular stacking of BLG, the Bernal stacking, and treat that simpler system first. At last, we study the arbitrary arrangement of BLG, the tBLG. We follow the work done by [15,16], and construct a continuum low-energy effective Hamiltonian, which is valid for twist angles  $\theta$ .  $10^\circ$  and independent of the structure being commensurate or incommensurate.

The valence and conduction bands of graphene touch each other at the K and K' points of the Brillouin Zone and follow a linear dispersion for low energies.

### 2.1 Band structure of SLG

We choose the reference frame for hexagonal lattice as in Fig. 2.1 and so describes the possible positions for the unit cells of this system:

$$\mathbf{R}_{n_1, n_2} = n_1 \mathbf{a}_1 + n_2 \mathbf{a}_2, \quad n_1, n_2 \in \mathbb{Z}, \text{ where } n_i = 0, 1, \dots, N_i - 1$$

with the primitive vectors being:

$$\mathbf{a}_1 = a_{\text{hex}} \left( \frac{1}{2}, \frac{\sqrt{3}}{2} \right), \quad \mathbf{a}_2 = a_{\text{hex}} \left( \frac{1}{2}, -\frac{\sqrt{3}}{2} \right) \text{ with } a_{\text{hex}} = \sqrt{3}d \quad (2.1)$$

where d is the carbon-carbon distance.

Among the 4 valence electrons of a Carbon atom, 3 are involved in strong in-plane covalent bonding while the remaining electron is delocalized in  $p_z$  orbital. Here we shall consider this electron within the regime of tight binding model with Nearest Neighbour hopping and construct a continuum model.

According to Bloch's theorem, the wave function for an electron in a periodic crystal has the form of a Bloch wave,

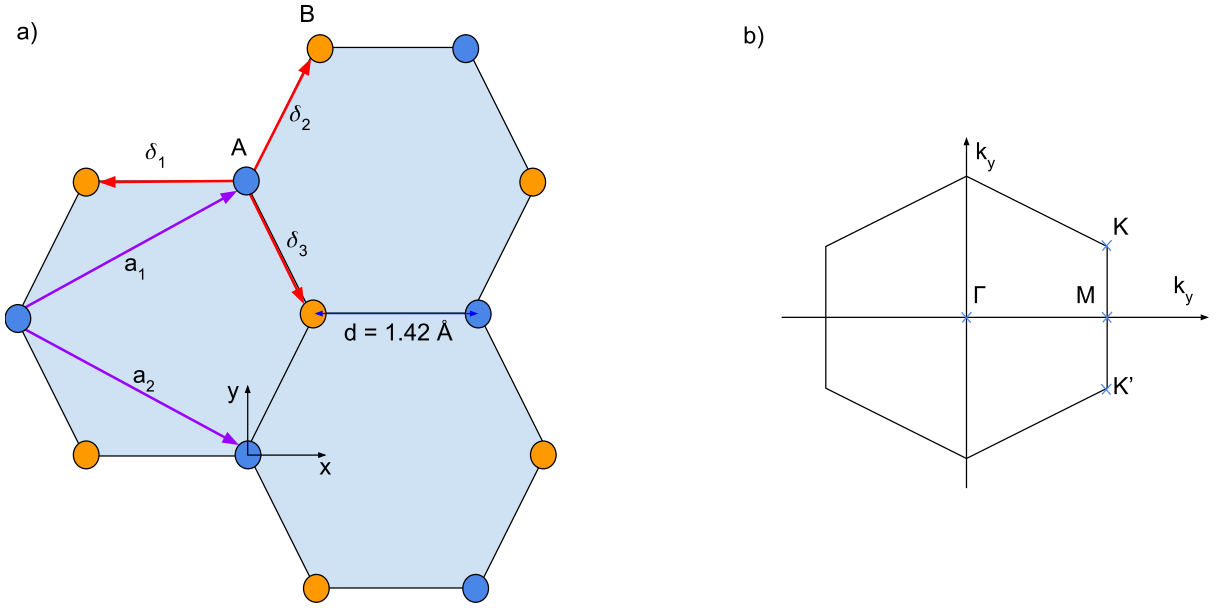


Figure 2.1: Reference Frame for Graphene Crystal: a) The honeycomb structure can be seen as two interpenetrating hexagonal lattices, A (blue) and B (orange). Its experimental structure parameter,  $d = 1.42 \text{ \AA}$  is also the C-C distance [4]. b) First Brillouin Zone of graphene denoting the K and K' Dirac points.

$$\psi_{\mathbf{k}}(\mathbf{r}) = e^{i\mathbf{k}\cdot\mathbf{r}} u_{\mathbf{k}}(\mathbf{r}) \quad \text{with} \quad u_{\mathbf{k}}(\mathbf{r}) = u_{\mathbf{k}}(\mathbf{r} + \mathbf{R})$$

So that,

$$\psi_{\mathbf{k}}(\mathbf{r} + \mathbf{R}) = e^{i\mathbf{k}\cdot\mathbf{R}} \psi_{\mathbf{k}}(\mathbf{r})$$

Further, we consider the nearest neighbour Hamiltonian,

$$\hat{H} = \epsilon_{p_z} - t_1 \sum_{\langle i,j \rangle} (a_i^\dagger b_j + b_i^\dagger a_j) \quad (2.2)$$

where  $t$  is homogenous nonzero hopping term, only between nearest neighbours (NN), which considers the possibility of an electron hopping from an atom to its NN, and a diagonal term,  $p_z$ , reflecting the atomic energy of an electron in the  $p_z$  orbital in the absence of any other nuclei.  $i(j)$  represent sublattice sites  $A(B)$ , the operator  $a_i^\dagger(a_i)$  creates (annihilates) an electron at the A site, and similarly for  $b_i^\dagger(b_i)$ .

The summation may be rewritten for better clarity as,

$$\sum_{\langle i,j \rangle} (a_i^\dagger b_j + b_i^\dagger a_j) = \sum_{i \in A} \sum_{\delta} (a_i^\dagger b_{i+\delta} + b_i^\dagger a_{i+\delta})$$

Now treating the hopping term as a perturbation together with the normalized unperturbed Bloch wavefunction,

$$|\psi_{\mathbf{k},\alpha}\rangle = \frac{1}{\sqrt{N_1 N_2}} \sum_{n_1, n_2} e^{i\mathbf{k} \cdot (\mathbf{R}_{n_1, n_2} + \boldsymbol{\delta}_\alpha)} |\mathbf{R}_{n_1, n_2} + \boldsymbol{\delta}_\alpha, \alpha\rangle \quad (2.3)$$

where  $|\mathbf{R}, \alpha\rangle$  is the ket corresponding to an atomic orbital in position  $\mathbf{R}$  and sublattice  $\alpha = A, B$  and  $\boldsymbol{\delta}_\alpha$  is the vector that links the origin of the unit cell to its respective sublattice  $\alpha$  atom,

$$\boldsymbol{\delta}_A = \mathbf{0}, \boldsymbol{\delta}_B = \boldsymbol{\delta} = (-d, 0)$$

Since we have 2 atoms per unit cell, the total wave function should be written as,

$$|\psi_{\mathbf{k}}\rangle = \sum_{\alpha} c_{\alpha}(\mathbf{k}) |\psi_{\mathbf{k},\alpha}\rangle \quad (2.4)$$

where  $c_{\alpha}(\mathbf{k})$  is a complex constant and  $\|c_{\alpha}(\mathbf{k})\| = 1$

Now this NN tight-binding model yields the following non-null matrix elements:

$$\begin{aligned} \langle \mathbf{R}_{n_1, n_2}, A | H | \mathbf{R}_{n_1, n_2} + \boldsymbol{\delta} + \boldsymbol{\delta}_{NN}, B \rangle &= -t, \\ \langle \mathbf{R}_{n_1, n_2} + \boldsymbol{\delta}_\alpha, \alpha | H | \mathbf{R}_{n_1, n_2} + \boldsymbol{\delta}_\alpha, \alpha \rangle &= \epsilon_{p_z} \end{aligned} \quad (2.5)$$

where  $\boldsymbol{\delta}_{NN}$  are the vectors that, for any carbon of sublattice A, connect its NN from sublattice B,

$$\boldsymbol{\delta}_{NN} = \mathbf{0}, -\mathbf{a}_1, -\mathbf{a}_2.$$

### 2.1.1 Energy bands

In order to obtain the electronic spectrum, we use the Schrodinger equation for the states and apply the bras  $\langle \mathbf{R}_{n_1, n_2}, A |$  and  $\langle \mathbf{R}_{n_1, n_2} + \boldsymbol{\delta}, B |$  so that we end up with a closed system of equations that we conveniently write in a matrix form,

$$\begin{bmatrix} \epsilon_{p_z} & -tf(\mathbf{k}) \\ -tf^*(\mathbf{k}) & \epsilon_{p_z} \end{bmatrix} \begin{bmatrix} c_A(\mathbf{k}) \\ c_B(\mathbf{k}) \end{bmatrix} = E \begin{bmatrix} c_A(\mathbf{k}) \\ c_B(\mathbf{k}) \end{bmatrix} \quad (2.6)$$

where  $f(\mathbf{k}) = e^{i\mathbf{k} \cdot \boldsymbol{\delta}} (1 + e^{-i\mathbf{k} \cdot \mathbf{a}_1} + e^{-i\mathbf{k} \cdot \mathbf{a}_2})$ .

After redefining the zero energy such that it coincides with  $p_z$ , we get,

$$H(\mathbf{k}) = \begin{bmatrix} 0 & -tf(\mathbf{k}) \\ -tf^*(\mathbf{k}) & 0 \end{bmatrix} \quad (2.7)$$

with eigenvalues,

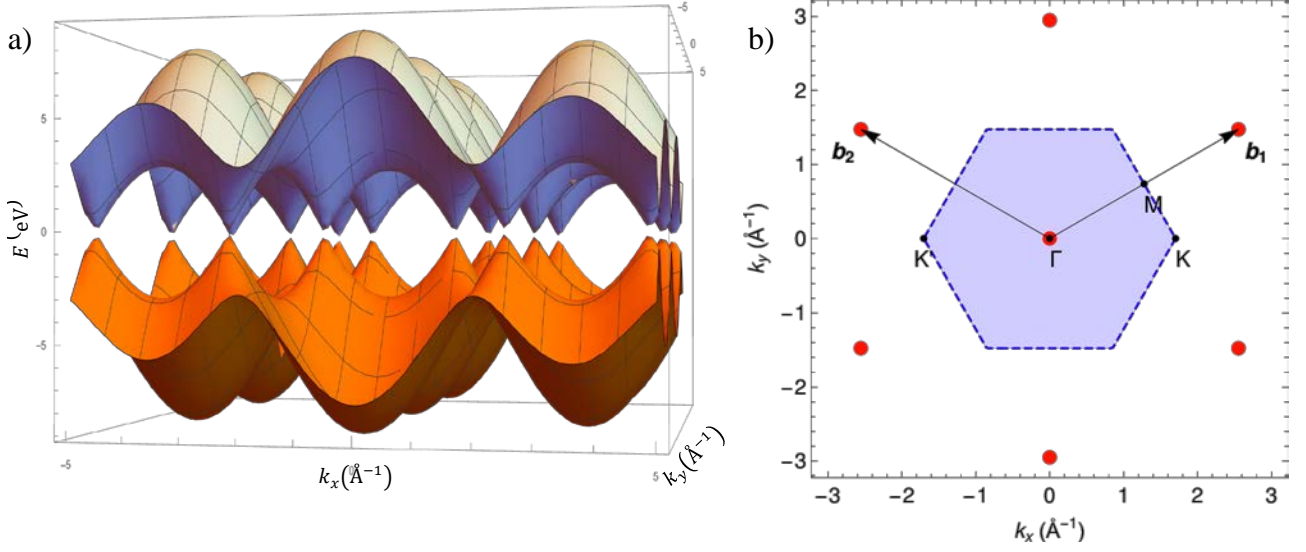


Figure 2.2: Energy Band in Graphene: a) Plot of Energy band in reciprocal space using Eq. 2.8. Tight-binding parameter was taken to be,  $t = 2.97\text{eV}$ , as taken from [10, 43]. b) is the corresponding Reciprocal space.

$$E(\mathbf{k}) = \pm t \sqrt{4 \cos\left(\frac{\sqrt{3}}{2} dk_x\right) \cos\left(\frac{3}{2} dk_y\right) + 2 \cos(\sqrt{3} dk_x) + 3} \quad (2.8)$$

These eigenvalues are used to model the conduction ( $\pi^*$ ) and valence bands ( $\pi$ ) in the reciprocal lattice space as shown in Fig. 2.2.

We can define the corresponding reciprocal lattice,

$$\mathbf{G}_{m_1, m_2} = m_1 \mathbf{b}_1 + m_2 \mathbf{b}_2, m_1, m_2 \in \mathbb{Z}$$

By definition,

$$\mathbf{a}_i \cdot \mathbf{b}_j = 2\pi \delta_{i,j}$$

which implies,

$$\mathbf{b}_1 = \left(\frac{\sqrt{3}}{2}, \frac{1}{2}\right) \frac{4\pi}{3d}, \quad \mathbf{b}_2 = \left(-\frac{\sqrt{3}}{2}, \frac{1}{2}\right) \frac{4\pi}{3d}$$

For completeness we may rewrite the Hamiltonian in reciprocal space through the following relation:

$$a_i^\dagger = \frac{1}{\sqrt{N/2}} \sum_{\mathbf{k}} e^{i\mathbf{k} \cdot \mathbf{r}_i} a_{\mathbf{k}}^\dagger$$

The effective mass of charge carriers is zero for a linear dispersion like graphene because, according to the band theory of solids, it is inversely proportional to the band curvature. The electrons

(and holes) in graphene can be used to investigate "relativistic condensed matter physics," providing an opportunity to examine physics that mimics QED (Quantum Electrodynamics) in table-top experiments. It also exhibits an extremely high Fermi velocity of  $10^6$  m/s. Klein tunnelling in graphene, one of this band structure's most exquisite characteristics [17, 18]. This is a counterintuitive relativistic phenomenon in which an incoming electron can flawlessly pass through a potential barrier if the barrier's height is greater than the electron's rest energy ( $m_e c^2$ ).

### Dirac-like Hamiltonian

A major regime of interest is in the low energy limit. This regime is found near the first BZ corners. We choose the two non-equivalent corners  $K_+$  and  $K_- = -K_+$  and make a Taylor series expansion of the Hamiltonian (Eq. 2.7) around them, obtaining, to the first nonvanishing order,

$$H_k = \begin{pmatrix} 0 & v_F [\hbar k_x - i \hbar k_y] \\ v_F [\hbar k_x + i \hbar k_y] & 0 \end{pmatrix} \quad (2.9)$$

where  $v_F$  is the Fermi velocity ( $\sim 10^6$  m/s), and diagonalize it obtaining the well-known eigenvalues:

$$E(k) = \pm v_F \hbar k \quad \text{where} \quad k = \sqrt{k_x^2 + k_y^2}$$

We can finally appreciate the conical shape of energy bands around  $K_-$  and  $K_+$  points, as well as the zero-energy gap nature and the relativistic behaviour of Dirac electrons in vicinity of Dirac point. This low-energy Hamiltonian is recognized as a (massless) Dirac-like Hamiltonian;  $K_+$  and  $K_-$  are thus called non-equivalent Dirac points.

It is useful to mention here that this is the exact same analysis that we shall partially outline for twist BLG in the following section to gain insights into the low energy continuum model as described by McDonalds, et. al. [19].

## 2.2 Bilayer Graphene

A BLG is a stacking of two SLGs, where the typical experimental interlayer distance is  $d_\perp = 3.35$  Å [5]. It can exist in three distinct arrangements:

- 1) AA stacking, where each carbon atom from the top layer is placed exactly above its correspondent in the lower layer;
- 2) AB stacking, or Bernal stacking, in which the atoms of sublattice A from one layer are aligned with the atoms of sublattice B from the other layer, implying the remaining to be located in the centre of the hexagons;
- 3) tBLG, where one layer is rotated by some angle  $\theta$  with respect to the other.

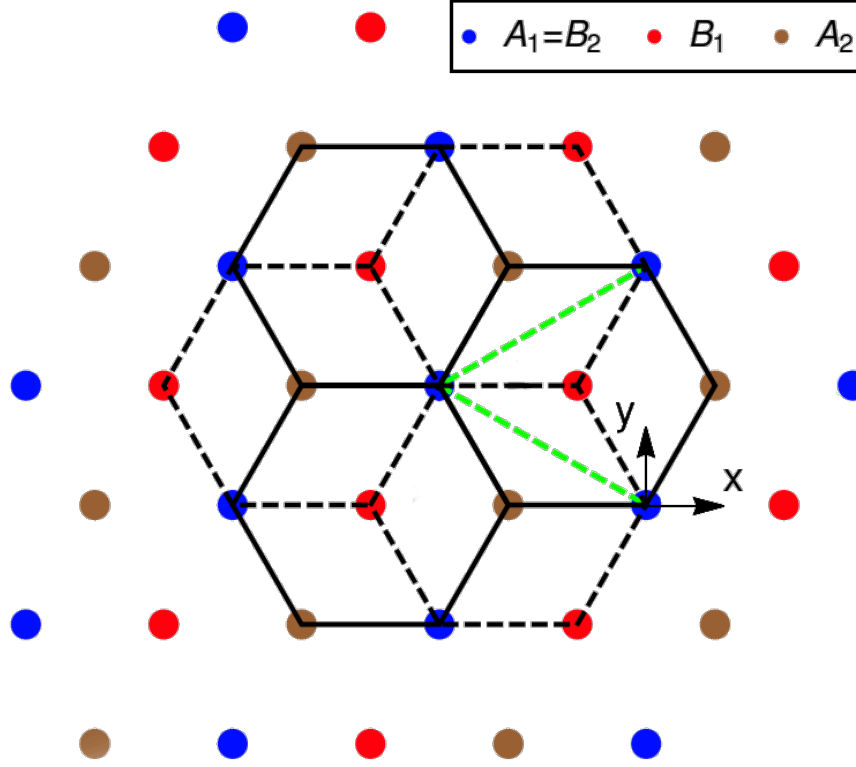


Figure 2.3: AB stacking BLG geometry (top view). We call the bottom layer (dashed black lines) layer 1 and the top layer (filled black lines) layer 2. We maintain the same unit cell used for the SLG (green dashed line), keeping both direct and reciprocal space descriptions identical as before, except that each unit cell now contains 4 atoms.

Experimentally, the AA stacking is considered metastable, while both AB stacking and tBLG are found to be stable [5]. In this section, we will focus on the AB stacking, whose geometry we show in Fig. 2.3.

The essential idea is to retain the approximations used before for each individual layer; while also considering interlayer hopping in a transversal tight-binding approximation between NN only. To keep the report, compact, we shall follow [20] closely and only highlight the important results.

The effective Hamiltonian now becomes,

$$H = H_1 + H_2 + H_{\perp}$$

where,

$$\begin{aligned} H_1 &= -t \sum_{n_1, n_2} \sum_{\sigma} a_{1, \sigma}^{\dagger}(\mathbf{R}_{n_1, n_2}) [b_{1, \sigma}(\mathbf{R}_{n_1, n_2}) + b_{1, \sigma}(\mathbf{R}_{n_1, n_2} - \mathbf{a}_1) + b_{1, \sigma}(\mathbf{R}_{n_1, n_2} - \mathbf{a}_2)] + \text{h.c.} \\ H_2 &= -t \sum_{n_1, n_2} \sum_{\sigma} a_{2, \sigma}^{\dagger}(\mathbf{R}_{n_1, n_2}) [b_{2, \sigma}(\mathbf{R}_{n_1, n_2}) + b_{2, \sigma}(\mathbf{R}_{n_1, n_2} - \mathbf{a}_1) + b_{2, \sigma}(\mathbf{R}_{n_1, n_2} - \mathbf{a}_2)] + \text{h.c.} \quad (2.10) \\ H_{\perp} &= t_{\perp} \sum_{n_1, n_2} \sum_{\sigma} a_{1, \sigma}^{\dagger}(\mathbf{R}_{n_1, n_2}) b_{2, \sigma}(\mathbf{R}_{n_1, n_2}) + \text{h.c.} \end{aligned}$$

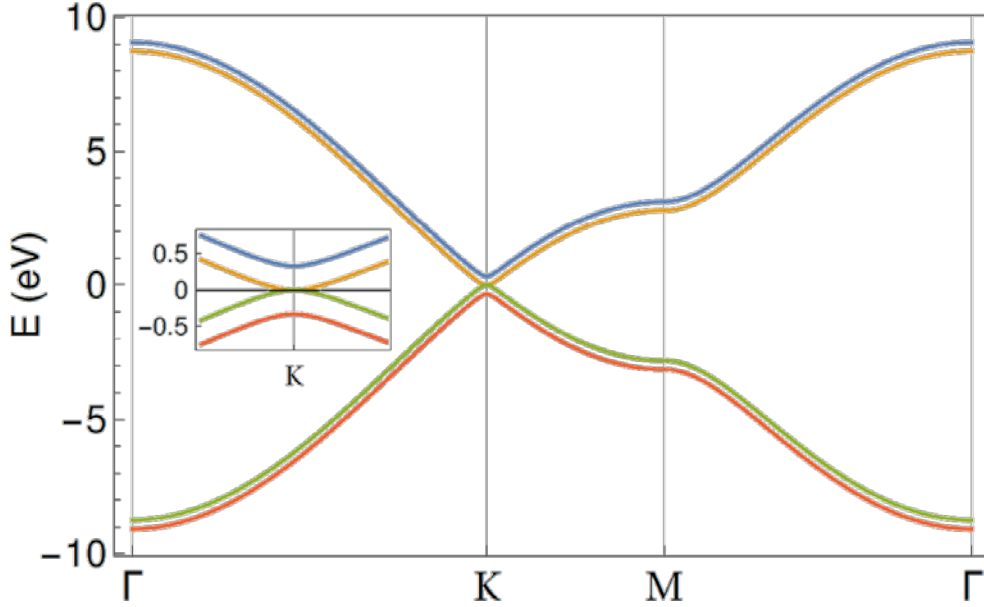


Figure 2.4: Electronic spectrum for AB stacking BLG, along the k-space trajectory  $\Gamma \rightarrow K \rightarrow M \rightarrow \Gamma$ . We set  $t_{\perp} = 0.33$  eV, compatible with the range of estimated values. [5]

clearly following the motivation from SLG calculation (Sec. 2.1.1).

### 2.2.1 Band Structure for Bernard Stacking

In the Reciprocal space, the total Hamiltonian becomes,

$$H = -t \frac{A_{\text{total}}}{(2\pi)^2} \sum_{\sigma} \int_{BZ} d\mathbf{k} \left[ \begin{array}{c} a_{1,\sigma}^{\dagger}(\mathbf{k}) b_{1,\sigma}(\mathbf{k}) f(\mathbf{k}) \\ + a_{2,\sigma}^{\dagger}(\mathbf{k}) b_{2,\sigma}(\mathbf{k}) f(\mathbf{k}) - a_{1,\sigma}^{\dagger}(\mathbf{k}) b_{2,\sigma}(\mathbf{k}) \frac{t_{\perp}}{t} + \text{h.c.} \end{array} \right] \quad (2.11)$$

where  $A_{\text{total}}$  is the total area of the unit cell.

Rewriting this in a convenient form we get,

$$H = \frac{A_{\text{total}}}{(2\pi)^2} \sum_{\sigma} \int_{BZ} d\mathbf{k} \Psi_{\sigma}^{\dagger}(\mathbf{k}) H(\mathbf{k}) \Psi_{\sigma}(\mathbf{k})$$

where,

$$\Psi_{\sigma}(\mathbf{k}) = \begin{bmatrix} a_{1,\sigma}(\mathbf{k}) \\ b_{1,\sigma}(\mathbf{k}) \\ a_{2,\sigma}(\mathbf{k}) \\ b_{2,\sigma}(\mathbf{k}) \end{bmatrix} \quad \text{and} \quad H(\mathbf{k}) = -t \begin{bmatrix} 0 & f(\mathbf{k}) & 0 & -t_{\perp}/t \\ f^*(\mathbf{k}) & 0 & 0 & 0 \\ 0 & 0 & 0 & f(\mathbf{k}) \\ -t_{\perp}/t & 0 & f^*(\mathbf{k}) & 0 \end{bmatrix}$$

Further diagonalizing, we get the eigen values as,

$$E(\mathbf{k}) = \pm t \sqrt{\left(\frac{t_{\perp}}{2t}\right)^2 + 4 \cos\left(\frac{\sqrt{3}}{2} dk_x\right) \cos\left(\frac{3}{2} dk_y\right) + 2 \cos(\sqrt{3} dk_x) + 3} \pm \frac{t_{\perp}}{2} \quad (2.12)$$

### Low-energy Limit

For the sake of completeness, the corresponding low energy limit is,

$$H(\mathbf{q}) = \hbar v_F \begin{bmatrix} 0 & \pm q_x - iq_y & 0 & \frac{t_\perp}{(\hbar v_F)} \\ \pm q_x + iq_y & 0 & 0 & 0 \\ 0 & 0 & 0 & \pm q_x - iq_y \\ \frac{t_\perp}{(\hbar v_F)} & 0 & \pm q_x + iq_y & 0 \end{bmatrix} \quad (2.13)$$

When we are interested in an (even lower) energy scale  $E \ll t_\perp$  we may neglect the high energy bands at  $E \sim \pm t_\perp$  (see the inset from Fig. 2.4) and work with an effective  $2 \times 2$  matrix Hamiltonian to get,

$$H^{\text{eff}}(\mathbf{q}) = -\frac{\tilde{p}^2}{2m^*} \boldsymbol{\sigma} \cdot \mathbf{n}(\pm 2\theta_q) \quad (2.14)$$

where  $\tilde{p} = \hbar|\mathbf{q}|$  is the momentum measured from the Dirac point,  $m^* = t_\perp/(2v_F^2)$  is recognized as the effective mass,  $\theta_q = \arg(q_x + iq_y)$  is the momentum orientation relative to the x-axis and  $\mathbf{n}(x) = (\cos(x), \sin(x))$  is a unitary vector.

As already mentioned, the most interesting part concerns  $K_-$  and  $K_+$  points where energy dispersion takes a quadratic shape while the conduction and valence bands touch each other in one single point preserving the nature of SLG, though with a non-vanishing effective mass since this time  $d^2E/dk^2 \neq 0$ .

### Opening BLG energy band gap

In contrast to monolayer graphene, it is possible to introduce an energy gap in bilayer graphene (BLG) by applying a displacement field between the two layers [21]. This distinct feature is highly beneficial for achieving electron confinement in this material. The tunability of the band gap in BLG has been observed in various experimental studies, including using external gates [22,23], scanning tunnelling spectroscopy [24], and magneto transport [25]. There are also numerous theoretical models available in literature [25, 26], which use tight-binding and Hartree theory to model this phenomenon.

#### 2.2.2 Periodic potentials in twisted bilayer graphene

A moiré superlattice can be obtained by twisting two sheets of materials with similar lattice constants. The lattice constant of the resulting superlattice is dependent on the relative rotation of the two sheets. In the case of identical materials, the superlattice can theoretically be extended to an infinite size. The relationship between the moiré wavelength and the relative rotation angle in a heterostructure composed of a graphene sheet and a material with dissimilar lattice constants is presented in Eq. 2.15,

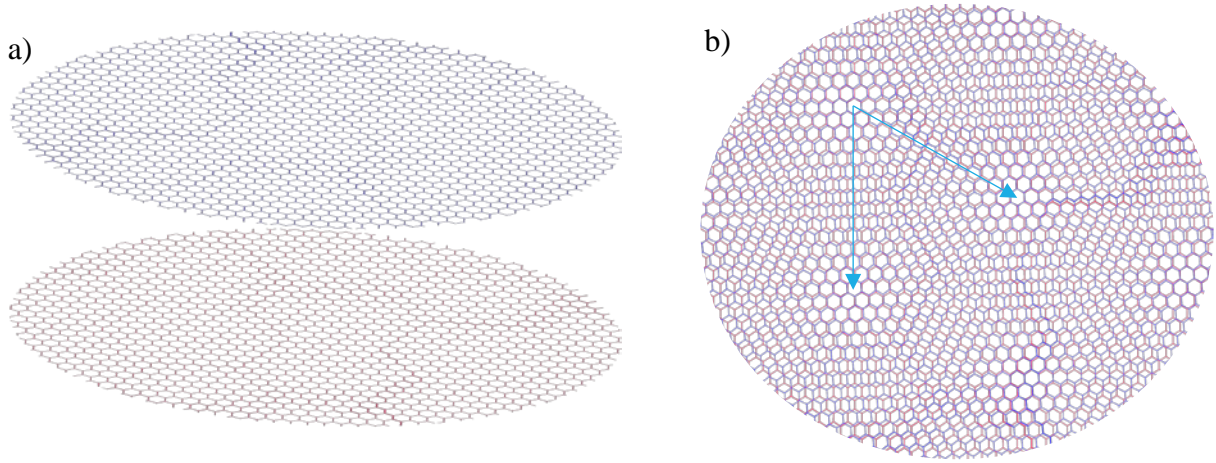


Figure 2.5: Moiré Pattern: a) side view of two hexagonal structure and b) corresponding top view. The arrow represent periodicity in the pattern.

where 'a' represents the lattice constant of graphene and ' $\theta$ ' represents the relative rotation angle, as demonstrated in reference [27].

$$\lambda = \frac{(1 + \delta)a}{\sqrt{2(1 + \delta)(1 - \cos \phi) + \delta^2}} \quad (2.15)$$

Twisted bilayer graphene has been the subject of extensive theoretical and experimental research following the isolation of graphene [28,29]. This system comprises two independently controlled graphene layers. The low energy physics of graphene is determined by non-zero K vectors, and a large relative twist between the two layers results in two distinct Fermi surfaces with minimal overlap. As a

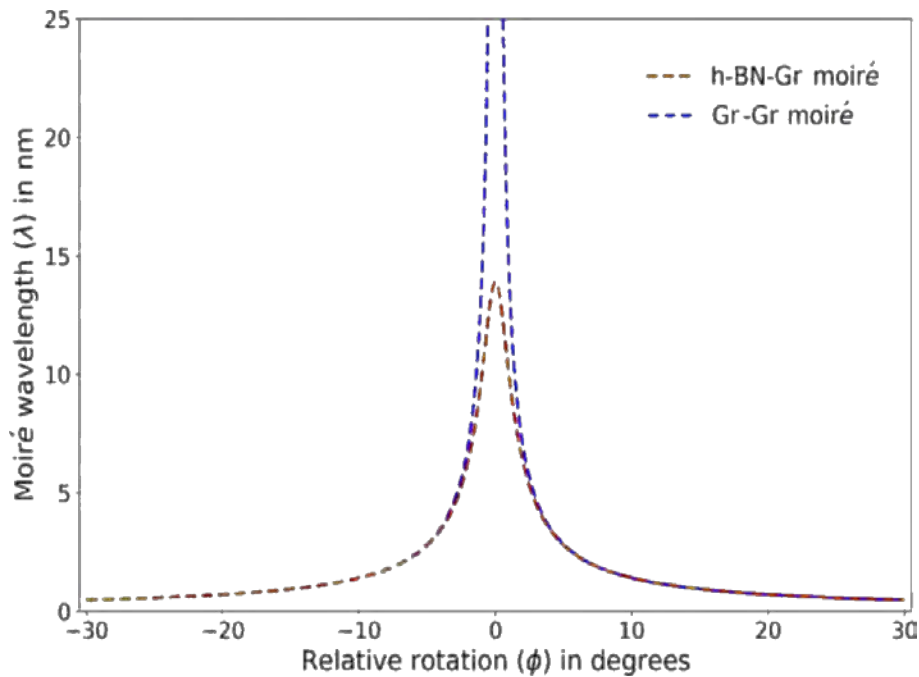


Figure 2.6: Moiré wavelength calculated from Eq. 2.5 for Gr-Gr and h-BN-Gr superlattices. Around zero angle mismatch, the Gr-Gr moiré wavelength diverges.

result, twice as many independent Dirac cones are obtained as in single-layer graphene, while preserving linear dispersion, a property for eg., was used to simultaneously realize two Quantum Hall states with opposite chirality. Quantum Hall states with opposing charge carriers but similar level doping will have opposite chirality (analogous to the Quantum Spin Hall effect in the presence of a magnetic field). Two single graphene layers with decoupled band structures within the same heterostructure provide this necessary feature of coexisting electron-like and hole-like band [30].

Theory of twisted BL being much more complicated and involved we shall simply outline the calculations here and present the numerical results as in [20].

Each layer is described by the following lattice:

$$\begin{aligned} \mathbf{R}_{n_1, n_2}^{(1)} &= n_1 \mathbf{a}_1 + n_2 \mathbf{a}_2 \\ \mathbf{R}_{n_1, n_2}^{(2)} &= R_\theta (n_1 \mathbf{a}_1 + n_2 \mathbf{a}_2 - \boldsymbol{\delta}) + \boldsymbol{\tau} \end{aligned} \Rightarrow \mathbf{R}_{n_1, n_2}^{(2)} = R_\theta (\mathbf{R}_{n_1, n_2}^{(1)} - \boldsymbol{\delta}) + \boldsymbol{\tau}$$

where  $R_\theta$  is the rotation matrix that describes an anti-clockwise rotation by  $\theta$  about the origin of a 2D coordinate system:

$$R_\theta = \begin{bmatrix} \cos(\theta) & -\sin(\theta) \\ \sin(\theta) & \cos(\theta) \end{bmatrix}$$

The idea is to start with a rotated Hamiltonian (within low limit regime) for SLG,

$$H_{SLG}^{\pm K}(\mathbf{q}, \theta) = \pm \hbar v_F |\mathbf{q}| \begin{bmatrix} 0 & e^{\mp i(\theta_q + \theta)} \\ e^{\pm i(\theta_q + \theta)} & 0 \end{bmatrix}$$

Now the total Hamiltonian is, similar to the Bilayer case (Sec 2.2.1),

$$H = H_1 + H_2 + H_\perp$$

where this time  $H_\perp$  is non homogenous and depends on the twist angle between the two layers and the interlayer hopping term is,

$$T_{\mathbf{k}, \mathbf{k}'}^{\alpha, \beta} = \langle \psi_{\mathbf{k}, \alpha}^{(1)} | H_\perp | \psi_{\mathbf{k}', \beta}^{(2)} \rangle$$

which, using the SLG wavefunctions may be written as,

$$\begin{aligned} T_{K+q_1, K^\theta+q_2}^{\alpha, \beta} &= \frac{1}{N_1 N_2} \sum_{n_1, n_2} \sum_{n'_1, n'_2} e^{-i(K+q_1) \cdot (\mathbf{R}_{n_1, n_2}^{(1)} + \boldsymbol{\delta}_\alpha^{(1)})} e^{i(K^\theta+q_2) \cdot (\mathbf{R}_{n'_1, n'_2}^{(2)} + \boldsymbol{\delta}_\beta^{(2)})} \\ &\times \langle \mathbf{R}_{n_1, n_2}^{(1)} + \boldsymbol{\delta}_\alpha^{(1)}, \alpha | H_\perp | \mathbf{R}_{n'_1, n'_2}^{(2)} + \boldsymbol{\delta}_\beta^{(2)}, \beta \rangle \end{aligned}$$

were,

$$\left\langle \mathbf{R}_{n_1, n_2}^{(1)} + \boldsymbol{\delta}_\alpha^{(1)}, \alpha | H_\perp | \mathbf{R}_{n'_1, n'_2}^{(2)} + \boldsymbol{\delta}_\beta^{(2)}, \beta \right\rangle = t_\perp \left( \mathbf{R}_{n_1, n_2}^{(1)} + \boldsymbol{\delta}_\alpha^{(1)} - \mathbf{R}_{n'_1, n'_2}^{(2)} - \boldsymbol{\delta}_\beta^{(2)} \right)$$

depends on distance between the atomic orbitals.

The key step involves calculation this term and showing that  $t_\perp$  is in fact periodic with the Moiré wavelength, as expected,

$$\tilde{t}_\perp(\mathbf{r}^{(1)}) = \sum_{\mathbf{r}^{(2)}} e^{-i\mathbf{k}' \cdot (\mathbf{r}^{(1)} - \mathbf{r}^{(2)})} t_\perp(\mathbf{r}^{(1)} - \mathbf{r}^{(2)})$$

To model  $t_\perp(\mathbf{r}^{(1)} - \mathbf{r}^{(2)})$ , we begin by expressing it via Slater-Koster parameters [31],  $V_{pp\sigma}$  and  $V_{pp\pi}$ , as follows:

$$t_\perp(\mathbf{r}^{(1)} - \mathbf{r}^{(2)}) = \cos^2(\gamma) V_{pp\sigma} \left( \sqrt{d_\perp^2 + |\mathbf{r}^{(1)} - \mathbf{r}^{(2)}|^2} \right) + \sin^2(\gamma) V_{pp\pi} \left( \sqrt{d_\perp^2 + |\mathbf{r}^{(1)} - \mathbf{r}^{(2)}|^2} \right)$$

where  $\gamma$  is the angle between the  $z$  axis and the line connecting  $\mathbf{r}^{(1)}$  to  $\mathbf{r}^{(2)}$ , and explore an exponentially-decreasing model [32] for  $V_{pp\sigma}$  and  $V_{pp\pi}$ ,

$$V_{pp\sigma}(r) = t_\perp \exp \left[ q_\sigma \left( 1 - \frac{r}{d_\perp} \right) \right], \quad V_{pp\pi}(r) = -t_\perp \exp \left[ q_\pi \left( 1 - \frac{r}{d_\perp} \right) \right]$$

These may be numerically solved and plotted (Fig. 2.7).

Following we shall now compile the results as predicted from [19]:

As the rotation angle is decreased, the interlayer coupling strength increases, resulting in hybridization of the Dirac cones and a decrease in the Fermi velocity. Hybridization of the neighbouring K points in the Brillouin zones of the two layers leads to a flattening of the low energy linear dispersion of graphene, resulting in a significant enhancement in the corresponding density of states (DOS). This is illustrated in Fig. 2.7. The superlattice edges are on the order of 13 nm for magic angle twisted bilayer graphene, compared to a lattice constant of 0.246 nm for single layer graphene, resulting in a comparatively smaller superlattice reciprocal wavevector.

The study further predicted a significant reduction in the Fermi velocity of twisted bilayer graphene for specific "magic angle" values, including 1.1°, 0.5°, 0.35°, 0.24°, and 0.2°, with the first of these angles later referred to as the "**magic angle**". This prediction was made possible by assuming that the interlayer tunnelling in TBG is determined by the moiré unit cell (as a function of twist angle) and not by individual constituent atoms.

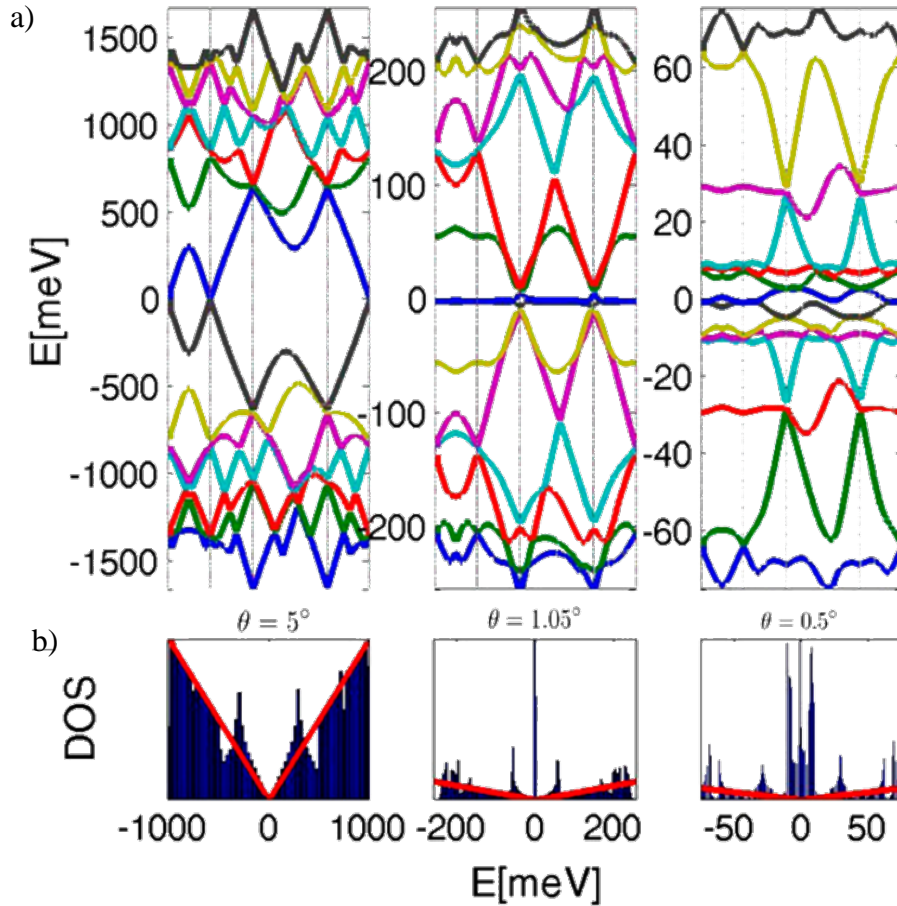


Figure 2.7: Moiré bands. a) Energy dispersion for the 14 bands closest to the Dirac point plotted along the k-space trajectory. b) DOS.

While typically there is a large barrier for electrons to tunnel between the layers, it was found that at these special angles, the barrier would become zero. This results in a drastic increase in interlayer tunnelling, leading to a slowing of the electrons in the same layer and the onset of interactions between them. Their band structure calculations also predicted the emergence of "**flat bands**" which are low energy bands with minimal dispersion. The presence of these flat bands leads to interesting phenomena such as the emergence of insulating states in a primarily metallic system. Notably, the possibility of superconductivity at the "magic angle" was not predicted. Additionally, they also calculated band structures for a few twist angles that showed a significant enhancement in the density of states (DOS) around the "first magic angle".

### 2.3 Correlated Insulators and Superconductivity in Magic Angle Twisted Bilayer Graphene

After Cao et al. [33] and Kim et al. [34] showed the existence of low energy bands separated from high energy dispersive bands by large energy gaps (also known as full filling gaps) in low angle twisted bilayer graphene. They first discovered insulating states at half filling of the flat bands in addition to

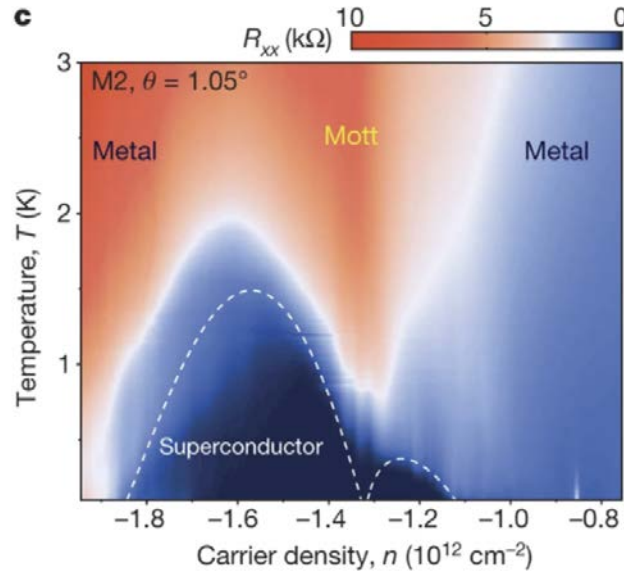


Figure 2.8: Unconventional Superconductivity in MATBG. The highest critical temperature measured is  $T_c = 1.7$  K. Taken from [52].

the previously observed full filling gaps. These half filling insulating states were attributed to electronic correlations at the magic angle, like Mott insulators. Near the half filling, unexpected jumps in conductance were also observed, and it became clear that these jumps were caused by superconductivity! What was more surprising was how closely spaced the superconducting and insulating phases were, akin to the phase diagram of high  $T_c$  superconductors. This observation led to an avalanche of research papers attempting to describe the origin of this superconductivity.

Superconductivity in TBG happens at astonishingly low electron(hole) densities of about  $2 \times 10^{12} \text{ cm}^{-2}$ , an order of magnitude lower than  $\text{LaAlO}_3/\text{SrTiO}_3$  interfaces and doped  $\text{MoS}_2$ , which themselves are orders of magnitude lower than other superconductors in terms of charge densities. To paint this picture in more concrete terms, superconductivity arises in TBG for 1 electron(hole)/100,000 carbon atoms!!

### 3. Experimental Fabrication Procedure

The formulation of a problem is often more essential than its solution.

Albert Einstein

Graphene is perhaps the most popular 2D material today, owing to its simplicity of production. The Van der Waals (vdW) materials [35, 36], on the other hand, which exhibit strong interatomic connections inside the 2D plane and weak vdW interactions between the layers atop one another [36], can be isolated into few layers thick or even monolayers. The true potential of vdW resides in the combining of layers that appear to be of diverse nature to create what is known as a heterostructure.

This chapter gives an overview of the heterostructure fabrication procedure used in our group. The basic idea is to fabricate an hBN encapsulated graphene nanostructure and then provide contacts for transport measurements on the device.

We discuss the fabrication methods of mesoscopic devices which involve a step-by-step procedure, starting from mechanical exfoliation of graphene flakes, their characterization via Raman spectroscopy and the vdW heterostructure assembly (called also stacking). The stack then undergoes post processing where more sophisticated processes like electron beam lithography (EBL), reactive ion etching (RIE) and molecular beam evaporation (MBE) to pattern and deposit edge contacts, which together with a top and bottom gate, can be used to cryo-measurements. Since the latter post processing part will remain the same, with no modifications, my work was solely on designing the fabrication steps for tBLG.

In this chapter, a typical van der Waals assembly as is done in our group is elaborated and subsequently in the next chapter, we elaborate the modifications to this workflow that was required to have a clean tBLG stack.

#### 3.1 Mechanical exfoliation

Graphene (hBN) flakes are exfoliated from natural graphite crystals - **NGS Naturgraphit GmbH** (hBN powder - **Momentive, grade PT110**) onto Si/SiO<sub>2</sub> (a layer of thickness ~ 300 nm of SiO<sub>2</sub> is grown thermal oxidation of Si substrate. The thickness can be precisely controlled by evaluating its apparent colour) substrates by using the scotch tape technique [37]. This method is specifically preferred for graphene exfoliation due to the superior quality flakes compared to other methods of producing graphene [4].

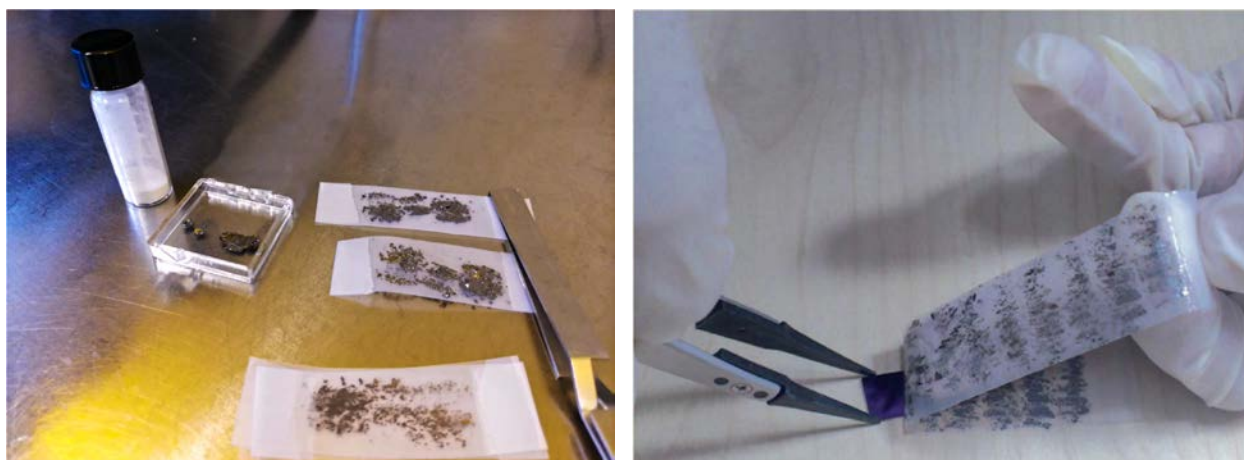


Figure 3.1: Mechanical Exfoliation: a) Exfoliation Inventory showing hBN powder in the bottle; graphite crystal and a few scotch tapes with exfoliated graphite. b) A step during exfoliation when the flakes are transferred onto the substrate.

Prior to exfoliation the Si/SiO<sub>2</sub> substrates are cleaned first by Ultra sonification to remove dust and other heavy contaminants, followed by dipping it into polar (double distilled water) and non-polar solvents (acetone and ethanol). For a better adhesion the substrate may then be Plasma treated in Oxygen (2 min exposure at 200 W, 0.2 mbar of Oxygen).

The idea of Mechanical exfoliation relies on the fact that the Van-Waals forces between the different layers are much weaker, and hence can be pulled apart into thinner flakes. Since we start with a tape containing highly dense flakes of different thickness, the number of exfoliations required to get an optimum result is found by trial and error and may range between 5-8 exfoliations starting from a fresh graphite crystal.

After several steps, the procedure is then completed by pressing the last tape to the silicon substrate with 300 nm SiO<sub>2</sub> for few seconds, obtaining, among several graphite flakes, different SLG and BLG ones as well. Fig. 3.1 presents the step when the exfoliated graphite on scotch tape is transferred onto the substrate.

Despite its simplicity, mechanical exfoliation is not fully controllable, since we start with randomly thick flakes of graphite, the number, and the size of SLG, BLG and Multilayer flakes is also probabilistic.

### 3.2 Characterisation of 2D crystallites

The advantage of transferring the flakes onto Si/SiO<sub>2</sub> is that this substrate provides visual contrast under an optical microscope. The colour and transparency are used to identify suitable candidates, which are further confirmed by either a Raman spectroscopy (in case of graphene) or under an AFM

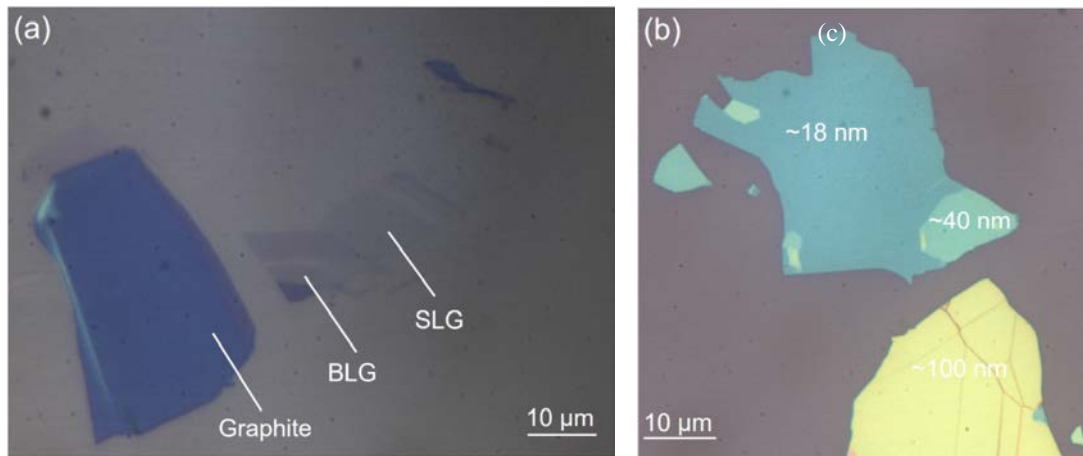


Figure 3.2: Contrast of flakes on Si/SiO<sub>2</sub> substrate: a) Graphite referred onto Si/SiO<sub>2</sub> substrate after exfoliation. Image shows the contrast difference under optical microscope. The thickness may be identified using either an AFM or Raman Spectroscopy b) exfoliated hBN flakes on substrate. Thickness is identified using AFM

(for hBN). The Fig. 3.2 shows the how the contrast is affected by thickness and acts as a reference for finding the required flakes.

The substrates contained a variety of flakes of different shapes, size, and thickness. We are interested in isolating single layer graphite (graphene) and hBN flakes having a thickness around 20 – 50 nm and especially on the flatness of their surfaces. This thickness of hBN is found to be optimum for the following reasons:

- Advantages of thicker hBN encapsulation are it is much less likely get cracked during stacking; and good insulation from the surrounding
- Disadvantages include loss of sensitivity while AFMing the stack (to identify the location of graphene after encapsulation); modifications in etching and Molecular deposition and requirement of much higher voltage across the top and bottom gate during transport measurements.

The flakes identified by eye are further confirmed using a Raman Spectrum in case of few layers graphite (using an AFM is not recommended as the tip might scratch the graphene surface leading to crystal defects) or an AFM for thickness of hBN flake.

### 3.2.1 Raman Spectrum of Graphene

The three most intense features [38–40] to identify graphene are:

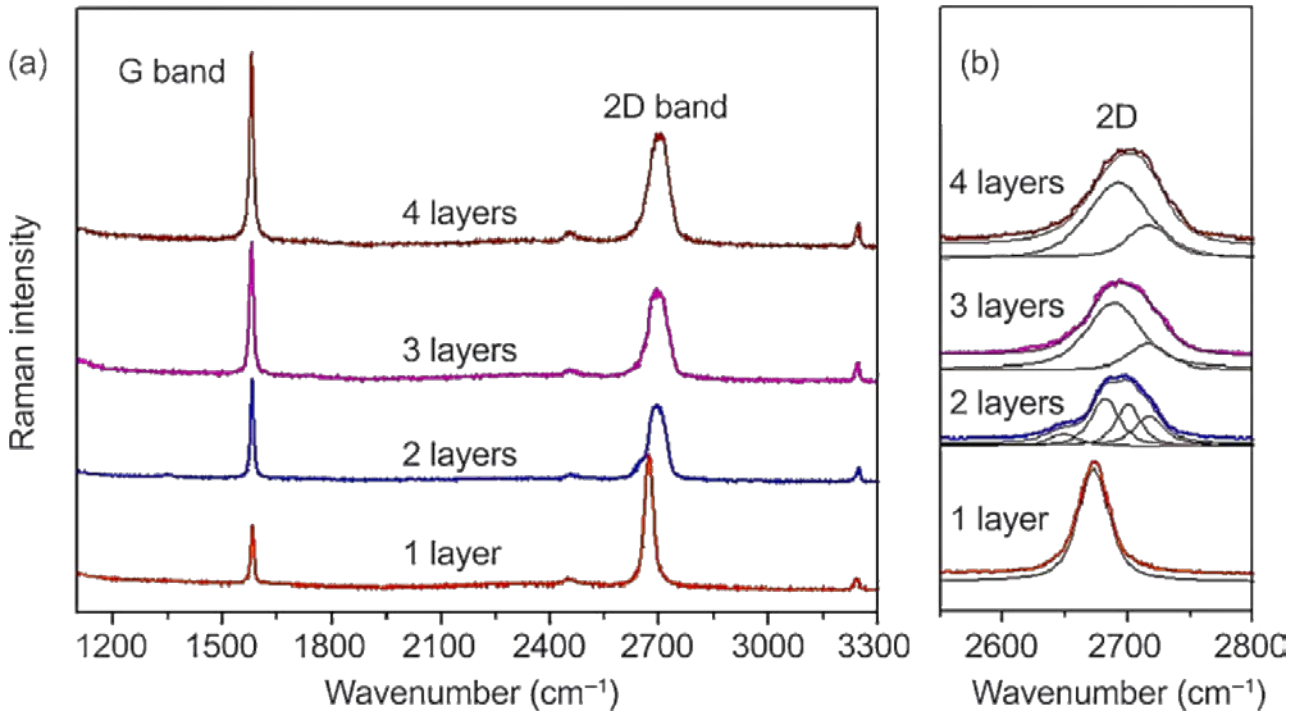


Figure 3.3: Raman Spectra of few layers graphene: a) Typical spectrum of up to 4-layer graphene. b) Shows the Lorentzian fit on the 2D peaks. The Spectra were obtained using Nd:YAG laser (532 nm) with a power below 0.1 W. [39]

1. A first order G peak at  $\sim 1583 \text{ cm}^{-1}$  (due to the doubly degenerate zone<sup>2</sup> center  $E_{2g}$  mode): In graphene, G position is  $3\text{--}5 \text{ cm}^{-1}$  higher than bulk graphite
2. D peak at  $\sim 1350 \text{ cm}^{-1}$  in defected graphite. Since zone-boundary phonons do not satisfy the Raman fundamental selection rule, they are not seen in first order Raman spectra of defect-free graphite. A finite D line response originating from the edges can be attributed either to defects or to the breakdown of translational symmetry.
3. G' peak (historical name) or the 2D peak  $\sim 2700 \text{ cm}^{-1}$  is due to the second order of zone-boundary phonons).
  - a. In bulk graphite consists of two components  $2D_1$  and  $2D_2$ , roughly  $1/4$  and  $1/2$  the height of the G peak, respectively.
  - b. In graphene, a single, sharp 2D peak in graphene, roughly 4 times more intense than the G peak.
  - c. the bilayer 2D band is not sharp as the monolayer counterpart but presents a multi component peak.

For more than 5 layers the Raman spectrum becomes hardly distinguishable from that of bulk graphite. Thus, Raman spectroscopy can clearly distinguish a single layer, from a bilayer from few (less than 5) layers.

<sup>2</sup> two-fold degeneracy (valence band and the conduction band are degenerate with zero energy).

### 3.2.2 AFM on hBN

The hBN thickness is confirmed by using AFM in tapping mode with default setting (Integral Gain is 0.5 and Proportional gain is 1.0) with tip speed as high as  $10 \mu\text{m s}^{-1}$ .

## 3.3 vdW heterostructure assembly

Heterostructure assembly is the process of stacking vdW materials one over the other. An important advancement in graphene based heterostructure was the discovery of hBN encapsulation as discussed below.

### 3.3.1 hBN encapsulation

The supporting substrate for graphene has a significant impact on the quality (mean free path and charge inhomogeneity at charge neutrality point) of graphene devices. In a sense, significant breakthroughs in graphene physics have been made as a result of the evolution of substrates for graphene since 2005. Prior to 2008, the widely used standard for high quality graphene devices was  $\text{SiO}_2$  [6, 41]. The creation of extraordinarily high mobility graphene samples with mean free  $> 2 \mu\text{m}$  [42] was then made evident by separating graphene from the substrate beneath by suspending which led to the observation of the fractional quantum hall effect in graphene [43, 44]. However, due to suspended graphene's propensity to collapse during the fabrication process or when a gate voltage is applied, these samples were particularly challenging to fabricate.

The field of graphene electronics was revolutionised [45] by the use of hexagonal Boron Nitride (h-BN) as a substrate because it gave graphene an atomically flat surface without charge puddles (unlike  $\text{SiO}_2$ ). With the aid of hBN, phenomena that had previously only been seen in a few suspended graphene devices have now been regularly observed.

One would not anticipate the substrate to have a significant impact on the physics of TBG given the chemical inertness of h-BN and the absence of any unusual electronic phases of its own. Historically, h-BN served as a substrate that decreased charge puddles and gave graphene an atomically flat surface, thus minimising electrical disorder. The 2-D honeycomb lattice of HBN exhibits a lattice constant that is strikingly similar to that of graphene. It is feasible to create a moiré wavelength of 14 nm (which is very similar to the moiré wavelength in Magic angle physics) when the two layers are perfectly aligned, which breaks the sublattice symmetry of the resulting heterostructure.

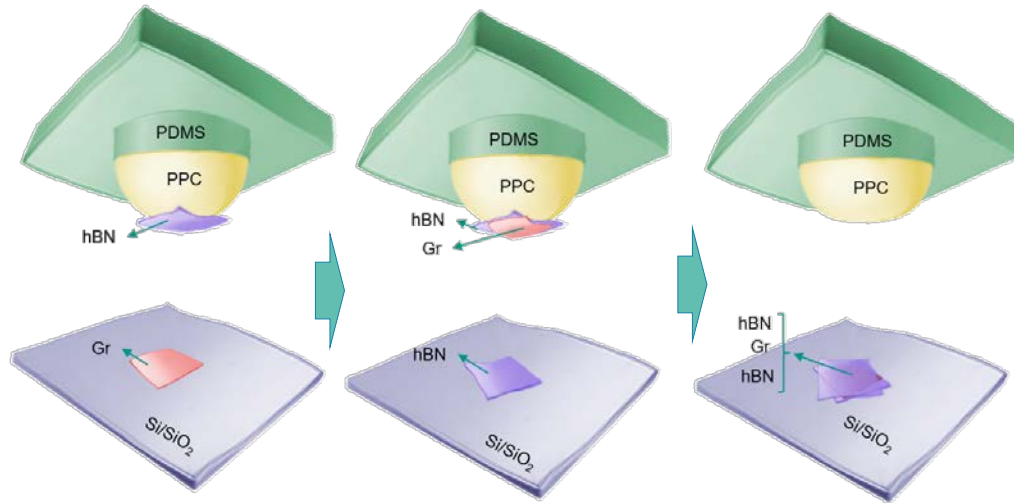


Figure 3.4: Illustration of van der Waals heterostructure assembly process as done in Danneau Group.

### 3.3.2 Dry stacking Technique

We follow the **Dry Stacking Technique** [46] which is the best way to get a clean stack (with as little contaminants as possible between the layers). The essential idea is to minimise direct contact with polymers (and for that matter anything other than that is necessary) as they are well known to leave residue. Hence, the best approach would be a *top-down procedure* where the polymer is only used to pick up the topmost layer first, using this layer pick up the second and so on.

For the sake of completion, we shall contrast this with the **Wet Stacking Process** that was prevalent. This takes a *bottom-up approach* where subsequent layers are picked up individually and

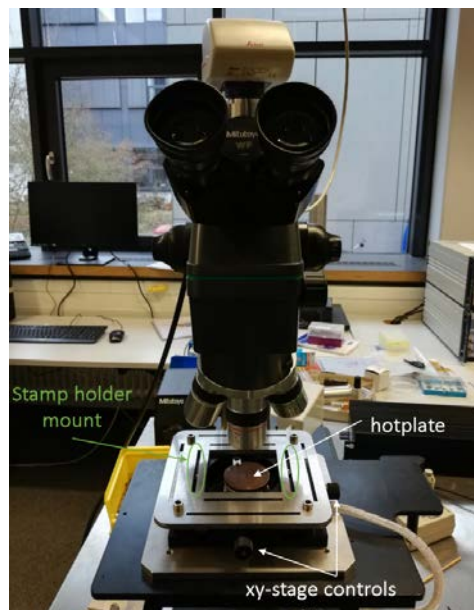


Figure 3.5: Stacking setup used for vdW assembly.

placed one above the other while cleaning the polymer using some solvent (hence the term wet) before placing another layer on top. Now, removal of the polymer from the interface is not perfect, and the decreased coupling due to the contaminants is well documented. [46]

We use a hemispherical stamp of polypropylene carbonate (PPC) on polydimethylsiloxane (PDMS) for improved adhesion to hBN [47]. A hemispherical stamp is preferred over spin-coating PPC because it is much easier to control the contact area and to later detach the stamp from substrate while pickup of flakes. (As elucidated in [Sec. 4.3.1](#), the rectangular PPC stamp made by spin coating is very hard to later detach from the substrate).

Our stacking setup is a home-made tele-microscope with a hot plate stage. The stamp is fixed onto the metal framing that can be independently moved in x-y direction (helps in positioning the stamp over the area of interest) while the sample is stuck to the hot plate which is movable in the z-axis (for contacting the stamp). The setup is shown in [Fig. 3.5](#).

The stamp is aligned over the hBN flake of interest using the objective where the hot plate is kept at room temperature. When the hemispherical stamp approaches the substrate Newton's Rings ([Fig. 3.6](#)) are formed which can be used to mark the first point of contact way before the stamp actually touches down. The substrate is pushed into the stamp until the whole flake is covered.

In order to melt PPC, the hot plate is warmed to  $\sim 60^\circ\text{C}$ , let to slowly cool down to room temperature. The pickup is completed by slowly pulling the substrate down thereby releasing the stamp, now containing the flake.

### 3.3.3 Dropping the stack from stamp

The commonly used method to drop the stack on the final hBN is by melting the polymer ( $\sim 100^\circ\text{C}$ ) fully onto the substrate followed by dissolving the PPC in acetone (later cleaned in isopropanol) and finally annealed at  $300^\circ\text{C}$  for 3 hr, since chemical dissociation in acetone is well known to leave residue.

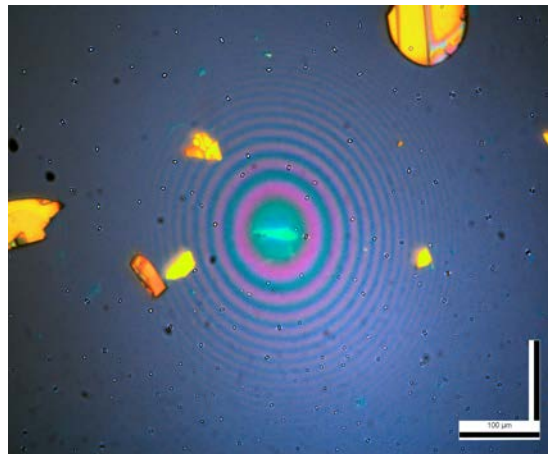


Figure 3.6: Newton's Ring Interference Pattern.

## 4. Modified Dry Stacking Procedure for tBLG

Whilst perfection is unrealistic, excellence can be attained by striving towards perfection.

Vince Lombardi

One would need to create a device with two layers of graphene stacked on top of each other and rotated by precisely  $\sim 1.1^\circ$  in order to verify the predictions made by MacDonald et al. [19]. Experimentally, this was quite difficult to accomplish because it requires two distinct graphene flakes with clearly defined axes. Now, the traditional methods for determining crystal axis involve doing an STM or e-beam diffraction on the flake. But that would be detrimental to the graphene flake. Due to the symmetry of honeycomb structure, an alternative way to determine the crystal axis would be to look at the edge structures. Fig. 4.1 represents the three among the several more ways a graphene can get torn. Fig. 4.1(a) and Fig. 4.1(b) are the naturally occurring edges as can be verified from the fact that the bond dissociations required to tear across a unit length is the minimum in these two cases, while Fig. 4.1(c) is yet another possible way, but does not occur naturally owing to a higher amount of bond dissociation energy required for the same unit length.

It is practically impossible to create a device with a perfect rotation of angle of  $1.1^\circ$  since graphene has two types of edges (zigzag and armchair). Late in 2015, a novel technique for producing precisely controlled twisted bilayer graphene was developed by two independent groups [33, 48].

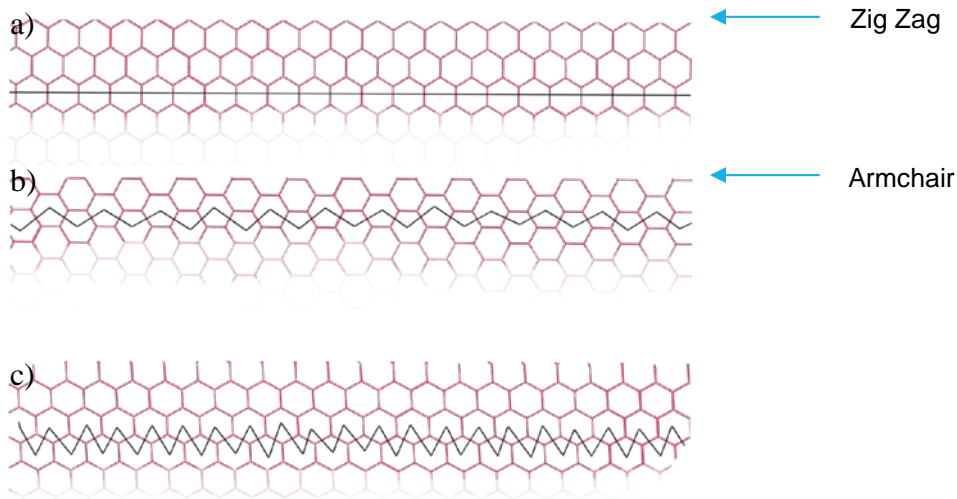


Figure 4.1: Edge of graphene. (a) and (b) are naturally occurring with equal probability while (c) does not occur in nature.

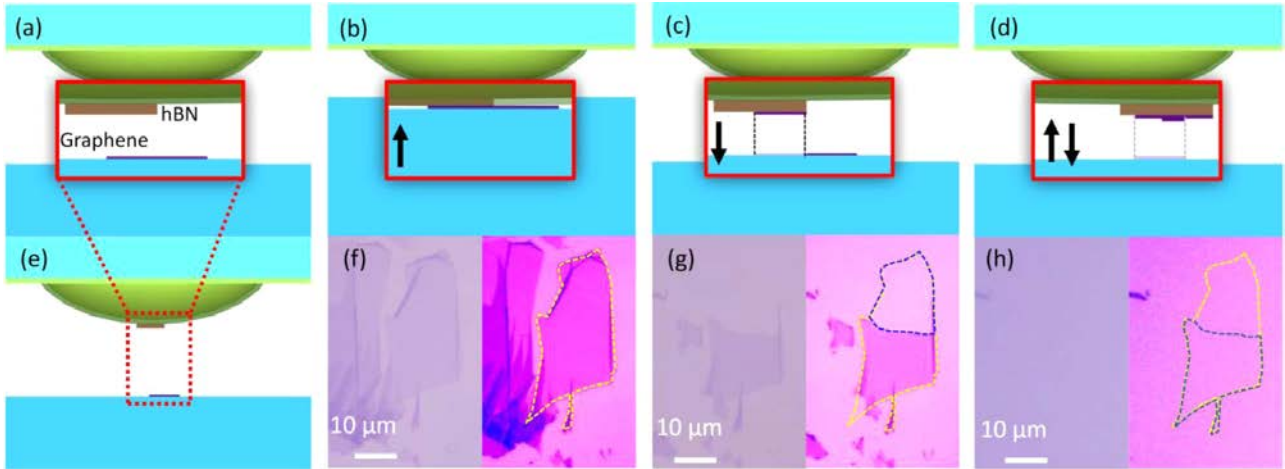


Figure 4.2: Rotationally aligned graphene double layer realized by successive transfers from a monolayer graphene using a hemispherical handle substrate.

The general procedure is represented in Fig. 4.2 instead of trying to find two different graphene flakes with well-defined edges, you would start with one big graphene flake (the nature of its edges does not matter). Then, an h-BN flake is brought into contact with part of the graphene flake. Upon lifting, the original graphene flake is "torn" and the part that was underneath the h-BN flake is picked up with the h-BN. This method utilizes the strong vdW forces between graphene and h-BN.

My primary aim for the thesis was to reproduce this method and replicate the twisted bilayer using tear and stack method. As we will point out soon, we found some inconsistencies with this exact procedure and was forced to take a novel detour to fix some of the inconsistencies.

The first hinderance was the fact that it turned out to be surprising hard to get a consistent tear yield with this seemingly simple procedure. We call this the tear Problem. The second obstruction was more serious and has to do with the unavoidable contamination on the second half of the graphene surface during the tearing process and we dub it the "clean interface problem".

This chapter is the main content of my thesis and deals with the principles applied and modifications used for a successful fabrication of tBLG. We start with the problem encountered when trying to apply the previous procedure and followed by explaining how each of these were tackled. The chapter concludes with an optimised step by step procedure to fabricate tBLG.

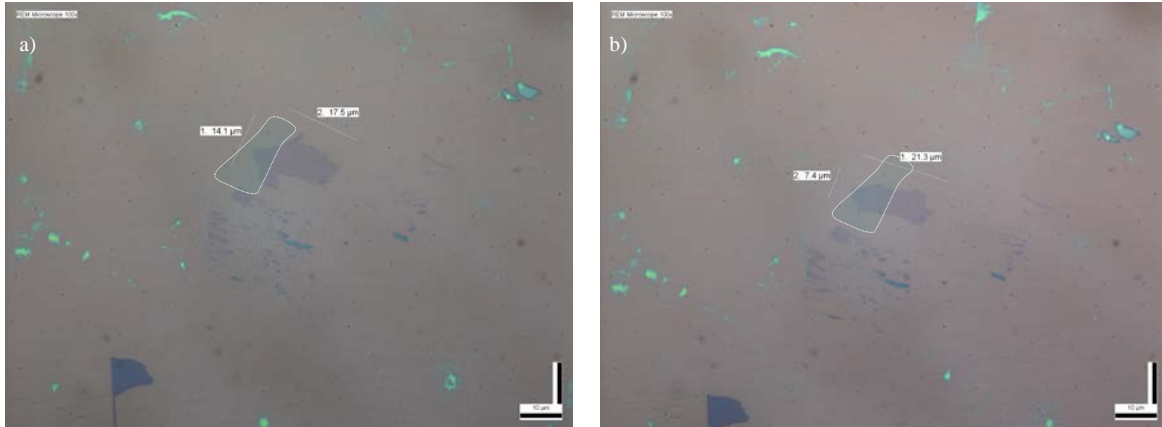


Figure 4.3: Tearing Problem: a) A graphene flake before pickup. b) Same flake after pickup contact with hBN. Faint outline is the contact region of hBN.

#### 4.1 Challenges for fabricating tBLG

Now a straight forward extension for tBLG would be to use the stamp with hBN flake to tear the graphene into two pieces by bringing down the hBN on only one half of the graphene flake and pulling it back up resulting in the graphene getting torn along the edge of the hBN.

Although this workflow is exceptionally efficient for a heterostructure stacking, it needs some modification because of the following problems that was encountered while fabricating a tBLG:

- **Clean Interface Problem:** A heat-cooldown cycle is found to be necessary when the stamp with hBN in contact with graphene flake prior to be able to pick the graphene. This heating would result in the PPC melting and spreading onto the other part of graphene, contaminating it. After all polymer not having to touch the graphene directly was the whole reason for success of dry stacking technique. This spread is found to be unavoidable when using a hemispherical stamp.
- **Tearing Problem:** Feasibility of being able to tear graphene with hBN has not been explored previously.

#### 4.2 Tear Problem

For example, the Fig. 4.3 shows a series image of a typical stacking trial. It was expected that the region of graphene under the hBN contact surface in Fig. 4.3(b) to be picked up by hBN as the literature claims and therefore should be empty, but clearly that is not the case.

Although the attempts were unsuccessful, some important conclusion could be drawn:

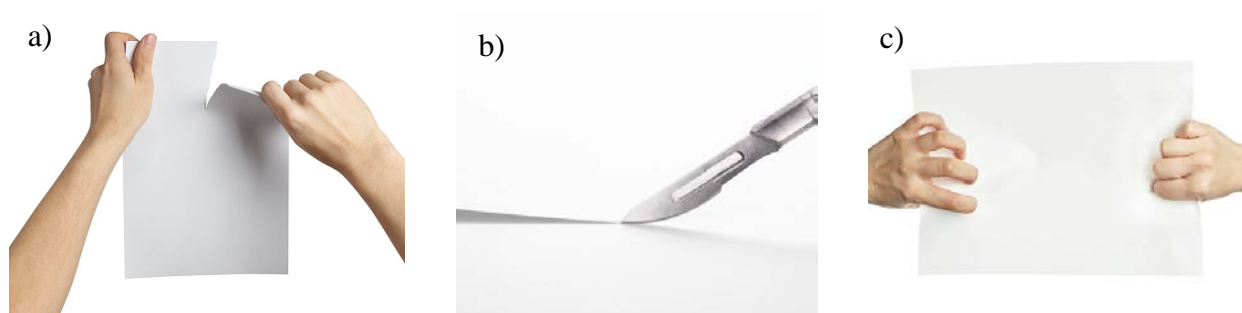


Figure 4.4: Tearing a Paper: a) Initiating the tear starting at an edge. b) Using a sharp object to tear. c) Pulling apart a paper.

- i. The technique of picking up graphene with hBN does not seem to be the trouble, it may be noticed on close inspection of [Fig. 4.3](#), that the top and bottom pieces of graphene within the hBN region have been picked up.
- ii. Furthermore, the regions that got picked up did have previous cracks along which the tear happened. i.e., the tear did happen, but only through the previously induced cracks, suggesting the fact that *initiating the tearing might be the problem*.

Hence, one might infer that tearing across the C-bonds is not easy and so to find a standard procedure it was clear that I needed to devise a technique to tear graphene reproducibly.

Here I explore these possibilities. The pivot point was in drawing analogy on how we tear a paper since graphene and paper share similarity in the sense that both are practically 2-dimensional. The idea is elaborated in the [Fig. 4.4](#) where three possible ways of tearing a paper are illustrated. [Fig. 4.4\(a\)](#) is the common way to tear a paper where you bend the paper in such a way to concentrate the tear force at a point on the edge and pull on the two sides to initiate the tear. [Fig. 4.4\(b\)](#) is yet another common way, where you use a sharp object to tear into two pieces. In both situations the common ground is the fact that you concentrate the tear force over a very small region until it gives away and then you continue to a neighbouring region.

To clarify a point, it is important to contrast [Fig. 4.4\(a\)](#) with [Fig. 4.4\(c\)](#). Although both look similar, the latter is where you try to rip apart a paper and the difference is that here the force is spread equally over the entire width and as expected requires much more tear force to be exerted in this case to breach the threshold stress and effectively rip it apart. Just to put this in perspective, a piece of paper that is half the width of an A4 sheet ( $\sim 10.5$  cm) can hold a weight of  $\sim 20$  kg before giving away [49], clearly indicating that situation in [Fig. 4.4\(c\)](#) is not efficient.

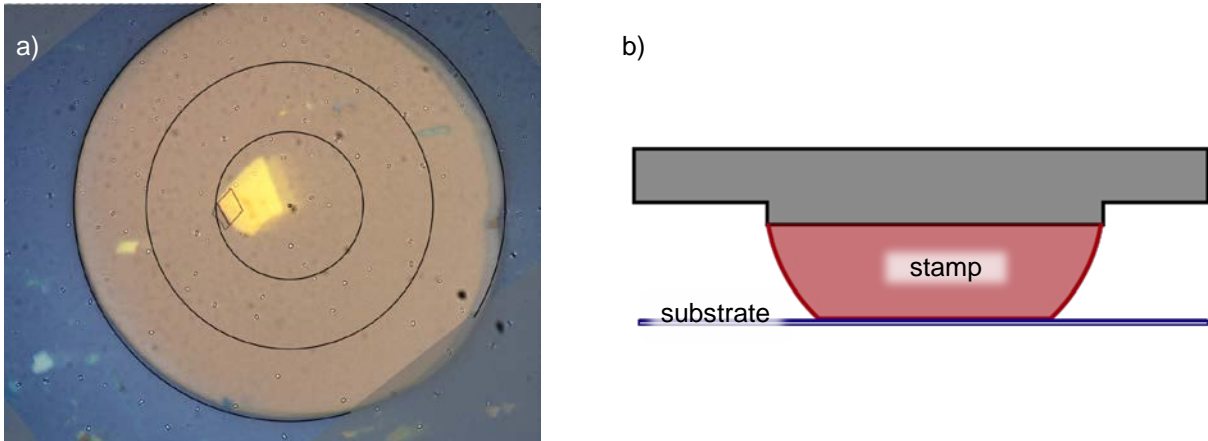


Figure 4.5: Tearing graphene using hBN: a) Optical image of the hBN in contact with first half of the graphene. Concentric circles and graphene tear outlines are overlaid. b) cross sectional schematic of (a).

We mimic the two most effective ways to tear a 2D material, this has the added advantage of knowing the involved physical principles. Drawing analogy from Fig. 4.4(a) and Fig. 4.4(b) for the former this involve optimizing the tear force to induce a tear and for latter a sharp tip such as that of an AFM is used to scratch across the graphene. In the following subsections we I explored both these possibilities.

#### 4.2.1 Tear using hBN flake

The idea here is to take advantage of the hemispherical shape and find an optimally curved region on the stamp to place the hBN to mimic the technique of tearing a paper by first bending in a way to concentrate the exerted force to a small region starting at an edge Fig. 4.4(a).

Fig. 4.5 is a successful attempt make at tearing the graphene using an hBN flake. Notice here that the hBN is not placed on the dead centre of the hemispherical stamp but rather to a side. The concentric circular overlay on Fig. 4.5(a) represents the sequential shrinkage of the contact edge when the stamp is pulled up. A second overlay at the edge of the hBN flake is the outline of graphene that was torn successfully along the edge of the hBN. Two important parameters, namely *how far the hBN is from the centre of the hemisphere* (helps with the curvature on hemisphere and mimics the bending of paper prior to tear) and *the angle the edge of the hBN makes with shrinking stamp edge* when releasing the stamp from the substrate (helps in applying a localised tear force that will eventually lead to the tear).

#### 4.2.2 Tear using AFM Tip

The simplest and fool proof way to tear a graphene is using an AFM tip in contact mode and scan along a line with Contact Setpoint set to greater than 1.2 V. To have a neat edge for later angle

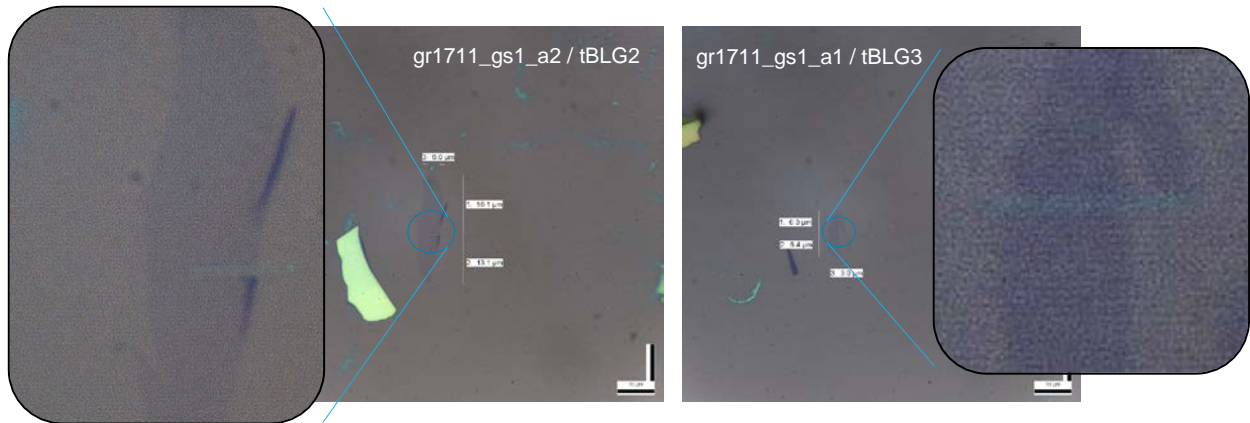


Figure 4.6: Graphene tore using AFM tip: The expanded window is the pixel zoomed image of the tear, which is clearly visible.

alignment it is recommended to keep the tip scan speed to less than  $3 \mu\text{m/s}$ . Fig. 4.6 represents two graphene flakes with an AFM tear at the centre. The gain factors and the exact value of the Contact Setpoint varies from tip to tip.

It is intriguing to observe that the silicon AFM tips used in this experiment quickly lost their sharpness; once they were dull, it was like tearing paper with a hammer. It is hardly surprising that the AFM tip is losing sharpness; after all, diamonds are cut with diamond cutters for a reason. Consequently, it is always recommended to use a fresh tip while cutting graphene using an AFM.

### 4.3 Clean Interface Problem

The problem here is that a hemispherical polymer stamp with hBN and you bring it down on only one half of the graphene. But then you have heat it up for better adhesion and this heating would also melt the polymer and cause it to spread on to the other half of the graphene and contaminating it. In more simpler terms the problem here is that the hemispherical polymer stamp starts to spread out after heating in an uncontrollable fashion. Fig. 4.7 is an illustration of the problem at hand.

Several approaches that could potentially minimise the heating cycle have been tried to solve this problem and due to lack of proper adhesive these had to be abandoned and the one that worked was by modifying the stamp shape. The idea was to modify the stamp shape to compensate for the various limitations of each shape.

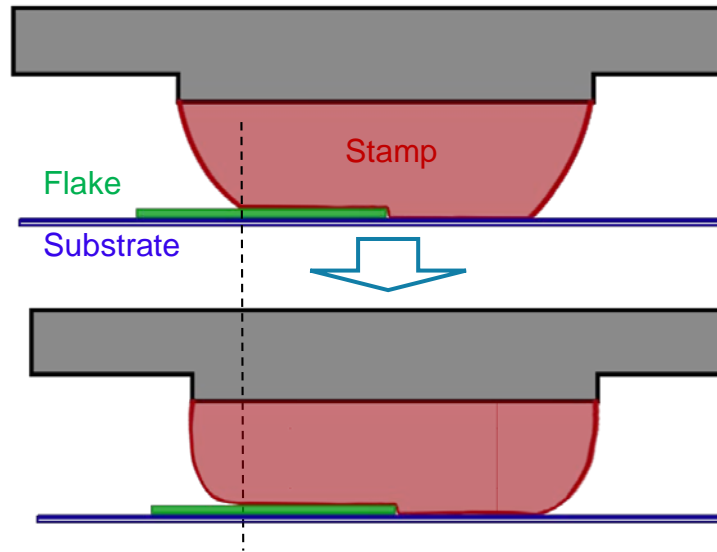


Figure 4.7: Schematic of the effect of heat on hemispherical stamp. The above cross-sectional sketch represents before heating and below is after heating. The dotted line contrasts the difference.

### 4.3.1 Rectangular Stamp

Table 4.1 shows three important features that is required for our setup and the most common types of stamps that can be easily produced. The convex / hemispherical stamp is known for being very easily detachable from substrate after contact while the concave case represents the other extreme that cannot be used for stacking owing to the neck that will break easily and is a problem when trying to detach.

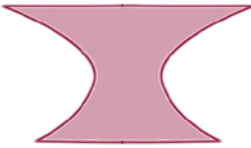
CONVEX	CONCAVE	RECTANGULAR
		
<ul style="list-style-type: none"> <li>✗ Contact edge expansion CAN be controlled</li> <li>✓ No NECK FORMATION and breakage</li> <li>✓ Easy to detach from substrate after contact</li> </ul>	<ul style="list-style-type: none"> <li>✓ Contact edge expansion CAN be controlled</li> <li>✗ No NECK FORMATION and breakage</li> <li>✗ Easy to detach from substrate after contact</li> </ul>	<ul style="list-style-type: none"> <li>✓ Contact edge expansion CAN be controlled</li> <li>✓ No NECK FORMATION and breakage</li> <li>✗ Easy to detach from substrate after contact</li> </ul>

Table 4.1: Comparison of Convex, Concave and Rectangular Stamp

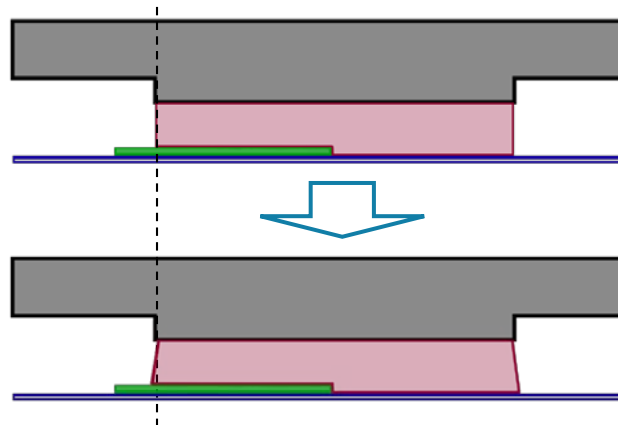


Figure 4.8: Schematic of the effect of heat on rectangular stamp. The above cross-sectional sketch represents before heating and below is after heating. The dotted line contrasts the difference.

The short side of a convex shape is that the edge expansion cannot be controlled since there is a huge bulk of polymer right above the edge is waiting to melt down with heating. This is not the case for the concave stamp as the edge has very little polymer and so the spreading is minimal. Now, the rectangular / cylindrical stamp can be thought of as the hybrid of these extreme cases.

Unfortunately, it turns out that the rectangular stamp is not easily detachable. Although the edge expansion by itself is not a problem, but that is sufficient to make the stamp much more adhesive to the substrate. The melt down causes the contact area on substrate to be more than that on the top and thereby making it more likely to stay stuck to the substrate when pulled back up.

CONVEX	RECTANGULAR	CONVEXO-RECTANGULAR
<ul style="list-style-type: none"> <li>✗ Contact edge expansion CAN be controlled</li> <li>✓ No NECK FORMATION and breakage</li> <li>✓ Easy to detach from substrate after contact</li> </ul>	<ul style="list-style-type: none"> <li>✓ Contact edge expansion CAN be controlled</li> <li>✓ No NECK FORMATION and breakage</li> <li>✗ Easy to detach from substrate after contact</li> </ul>	<ul style="list-style-type: none"> <li>✓ Contact edge expansion CAN be controlled</li> <li>✓ No NECK FORMATION and breakage</li> <li>✓ Easy to detach from substrate after contact</li> </ul>

Table 4.2: Comparison of Convex, Rectangular and Convexo-Rectangular stamps.

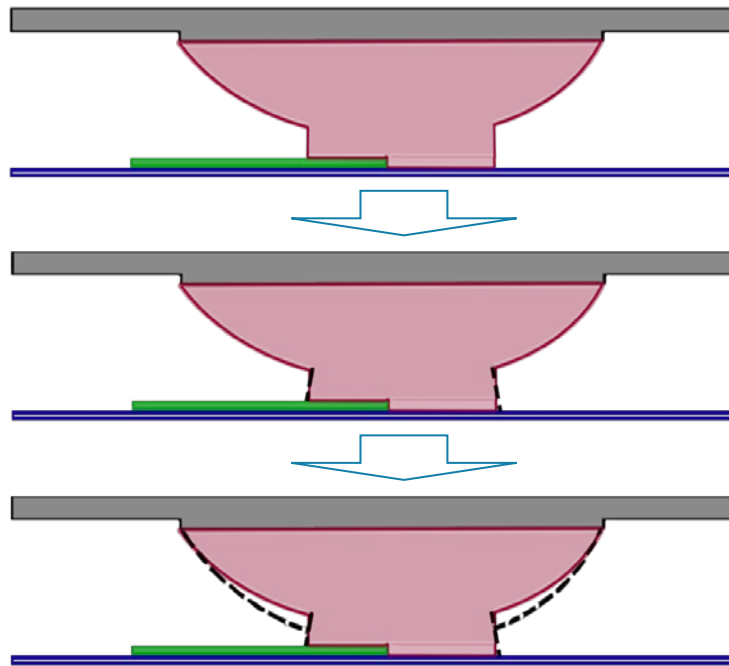


Figure 4.9: Schematic of the effect of heat on convexo-rectangular stamp. The above cross-sectional sketch represents before heating. The deformation due to melting would start at the base and is illustrated in the middle sketch. The bottom sketch is the melting of the convex part due to the eventual heat transfer.

### 4.3.2 Convexo-Rectangular Stamp

Now although we managed to contact the edge expansion with a rectangular stamp, the fact that it is not easy to detach from the substrate later makes it much more difficult to produce a consistent result.

The idea was again to combine the shapes having compensational features and hope that the hybrid shape is easy to create and more importantly inherit the best features from the two shapes. It turns out that constructing a convex / hemispherical stamp with a rectangular / cylindrical base, as shown in [Table 4.2](#), happens to satisfy all the criteria.

[Fig. 4.9](#) explains the reason behind why there is neither a neck formation nor the risk of stamp failing to detach. Although heating would cause the rectangular base to melt, the heat transfer to the convex part above will eventually lead to its deformation which compensates for the neck formation and the breakage there after that would have possibly happened.

To summarise this subsection, we have managed to find an optimal shape of the stamp that would help us avoid the spread of the polymer and the contamination of the other half of the graphene during

the stacking process, while at the same time making it considerably easy to handle this stamp throughout the process.

#### 4.4 Spectrum of Large angle tBLG

Raman Spectroscopy can be used to distinguish between large twist angle for bilayer graphene.

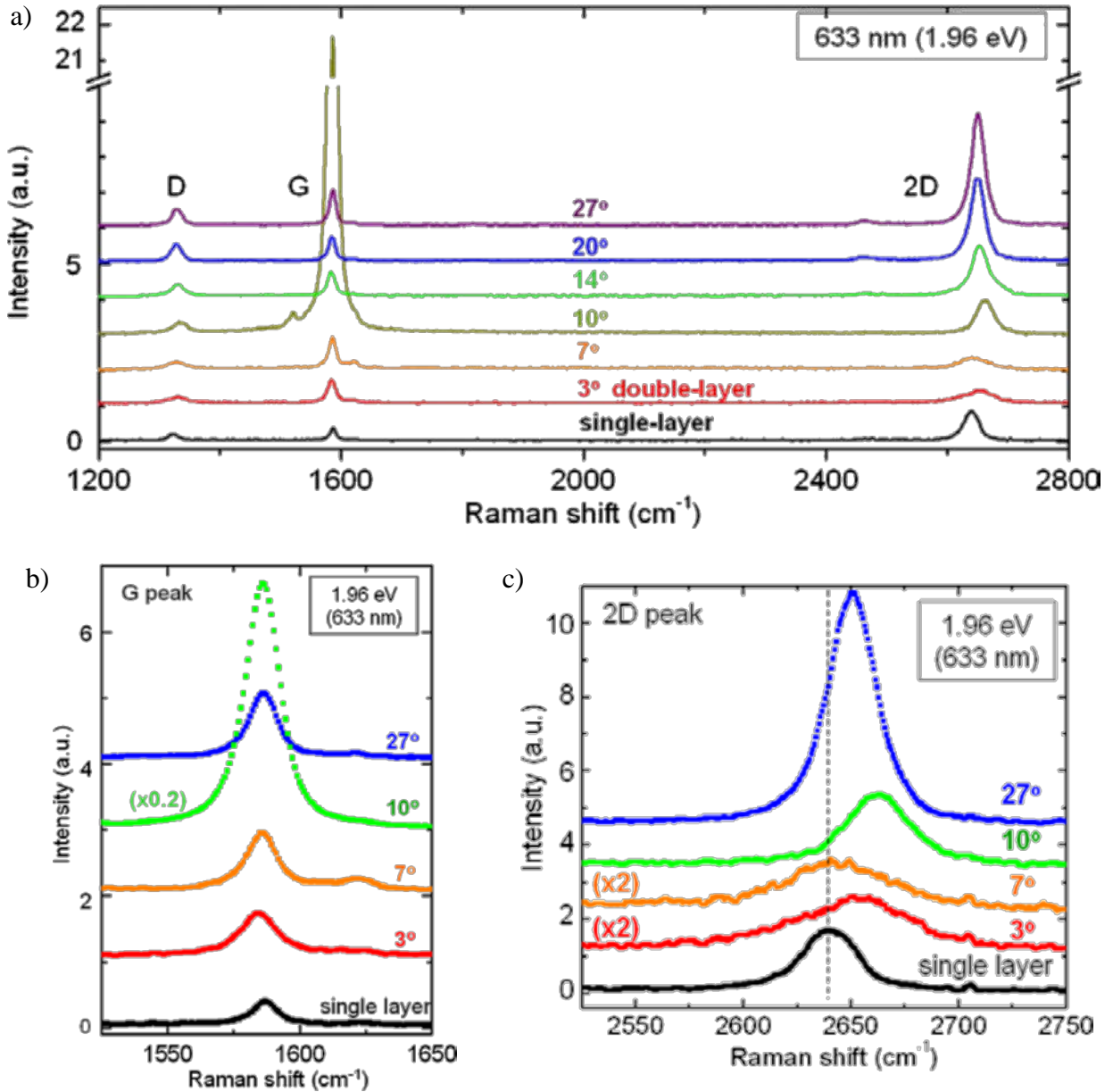


Figure 4.10: Raman Spectrum for LA tBLG: a) Complete Raman spectra b) G-peak and c) 2D- peak of tBL and SL graphene measured with 633 nm wavelength laser (1.96 eV). The spectra are shifted vertically for clarity. [50]

Misoriented double-layers with low angles ( $< \sim 8^\circ$ , for a 633 nm laser wavelength) show the Raman signal of a significant interaction between layers. The double-layers have Raman spectra that are more similar to those of single-layer graphene in the high angle regime ( $> 13^\circ$ ) as seen in Figure 4.10. When compared to monolayer graphene, the 2D peak of double-layer graphene exhibits a blue shift, with the amplitude of the blueshift being nonmonotonically dependent on the rotation angle. A high G peak resonance at  $\sim 10^\circ$  is also observed [50].

Hence, the angle may be identified by this blue shift in the 2D peak as well as the ratio between the G to 2D-peak.

#### 4.5 Post Cleaning Processes

The stacking process ends with the partial stack together with the PPC stamp being dropped onto the bottom hBN and later cleaned using Acetone. The need for Thermal annealing to remove residue seems to influence the Raman background<sup>3</sup> as evident from the Raman Spectrum in Fig. 4.11.

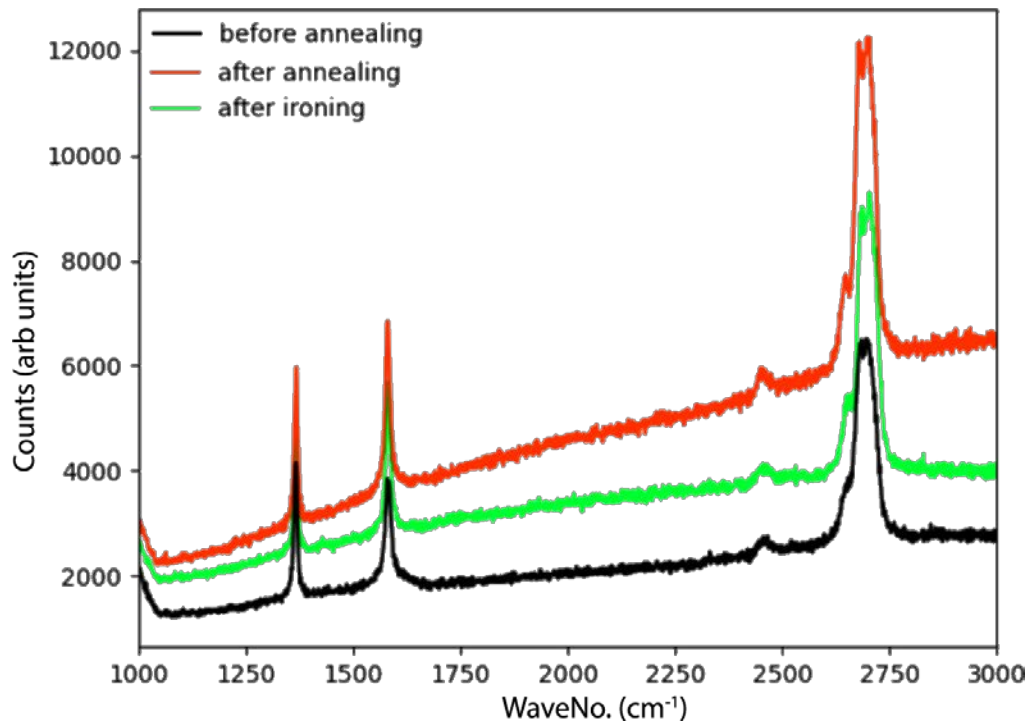


Figure 4.11: Effect of Annealing on Raman Spectrum. This is a BLG stack.

<sup>3</sup> This has also been reproduced in the thesis report of a previous student in our group - G. Di Maio

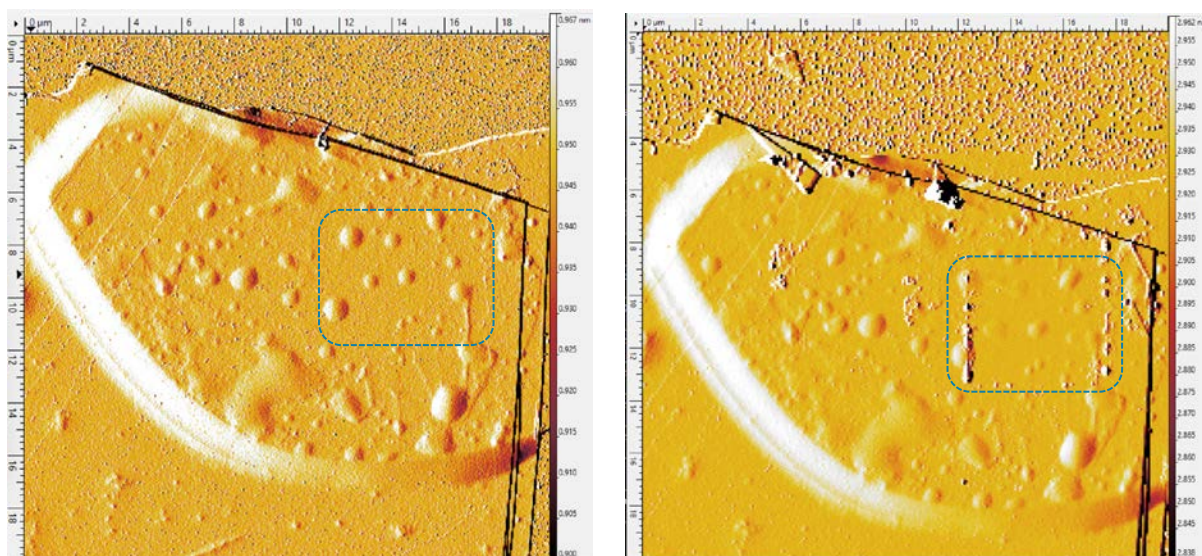


Figure 4.12: AFM Ironing: a) AFM of stack before ironing. b) Same stack after AFM Ironing

An alternative method following [51] was tried out where only the partial stack and not the PPC stamp was dropped onto the bottom hBN, was found to leave significantly less residue as seen from the Raman background Fig. 4.11. This could in turn revoke the need for a thermal annellation step. The procedure followed was to heat up the stack on stamp in contact with the bottom hBN to  $\sim 70\text{-}80^\circ\text{C}$  and then rapidly withdrawing the stamp. This is possible because adhesion of polymers like PPC is temperature-dependent [47].

Thermal annealing has the effect of agglomerating bubbles together. This can also be achieved by AFM Ironing which also pushes bubbles out of the way, as seen in Fig. 4.12, to consistently create larger bubble free area for device fabrication.

## 4.6 Results

This section is essentially a step-by-step optimized procedure to make twisted Bilayer Graphene. I shall gather the various aspects discussed earlier and condense it into the Modified Dry Stacking Procedure for tBLG:

STEP 1: Exfoliation of hBN and graphene flakes; and their characterisation using either an AFM or Raman spectroscopy.

STEP 2: Fabrication of a convexo-rectangular (Hemispherical stamp with a cylindrical plateau as it would look in 3D) stamp.

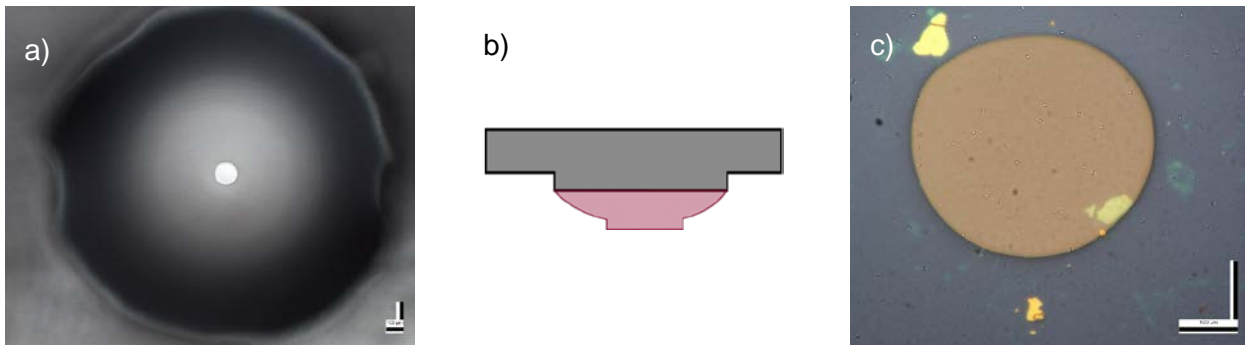


Figure 4.13: Convexo-rect. stamp. a) Optical image of hemispherical stamp with a cylindrical plateau at the tip and b) corresponding cross-section. c) is the optical image of (a) picking up an hBN flake.

This shape is a straight forward extension of the hemispherical stamp, where you start by putting a drop of PPC on the PDMS base using a Pipette and baking it at  $80^{\circ}\text{C}$  for  $\sim 20$  min. This is followed by pressing the stamp on a clean Si/SiO<sub>2</sub> substrate heating it setup to above glass transition temperature of PPC ( $\sim 50^{\circ}\text{C}$ ) and cooling it back close to room temperature and detaching the stamp from the substrate before it fully cools down.

This stamp left to fully cooldown will have an elongated cylindrical plateau at the centre (Fig. 4.13) which previously contacted the substrate.

#### STEP 3: Pickup of hBN for encapsulation.

hBN with a straight edge, that is later used to aligning the twist, and thickness  $\sim 20\text{-}40$  nm is identified and while pickup, it must be necessarily located very close to the edge of the cylindrical plateau to avoid the stamp spread out to the other half of the graphene ([4.3 Clean Interface Problem](#)). Fig. 4.13(c) shows the modified stamp in contact with the hBN for pickup.

The hBN flake is brought in contact with the stamp and the hot plate is heated to  $\sim 60^{\circ}\text{C}$  before slowly cooling down to room temperature and the stamp is withdrawn to pick up the flake.

#### STEP 4: Tear Graphene.

The fastest and the most efficient way to tear a graphene flake was found to be by using an AFM tip.

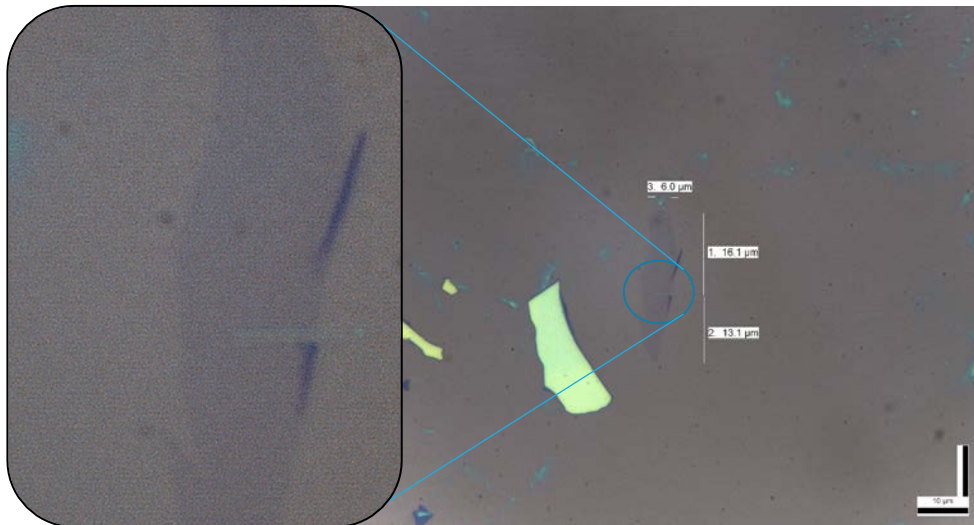


Figure 4.15: AFM tear of a graphene flake and the pixel zoomed in view

A graphene flake of height : width greater than 1:2 is first scanned in tapping mode to identify the middle to initiate the tear. After the scan area is zeroed on the centre, repeated scanning in contact mode along the centre is initiated which tears the graphene flake into two halves as shown in Fig. 4.14.

#### STEP 5: Pickup of the 1<sup>st</sup> Graphene Half.

The stamp with the hBN is aligned such that the straight edge of hBN is straight above the graphene tear, as shown in Fig. 4.15 which in turn will guaranty that the other half of graphene is outside the contact area of the stamp and hBN.

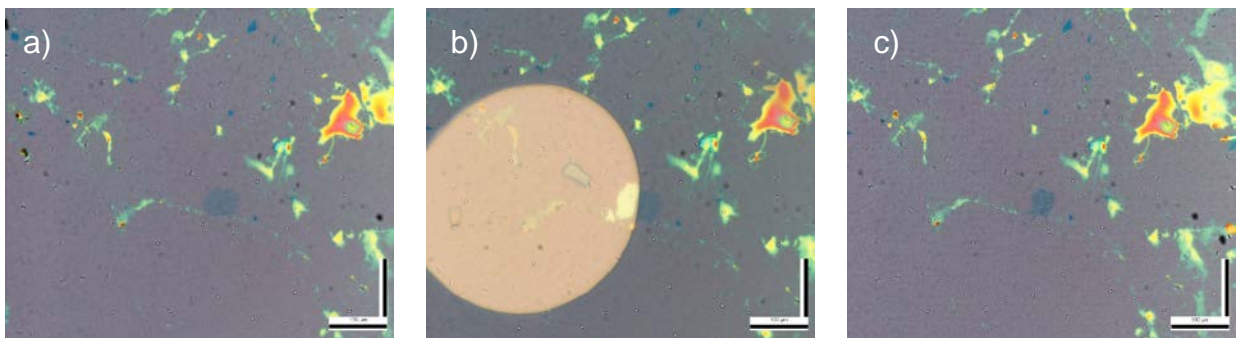


Figure 4.14: Optical image of a) graphene flake before tear-pickup, b) stamp with hBN in contact with half gr and c) other half of graphene left on substrate after tear.

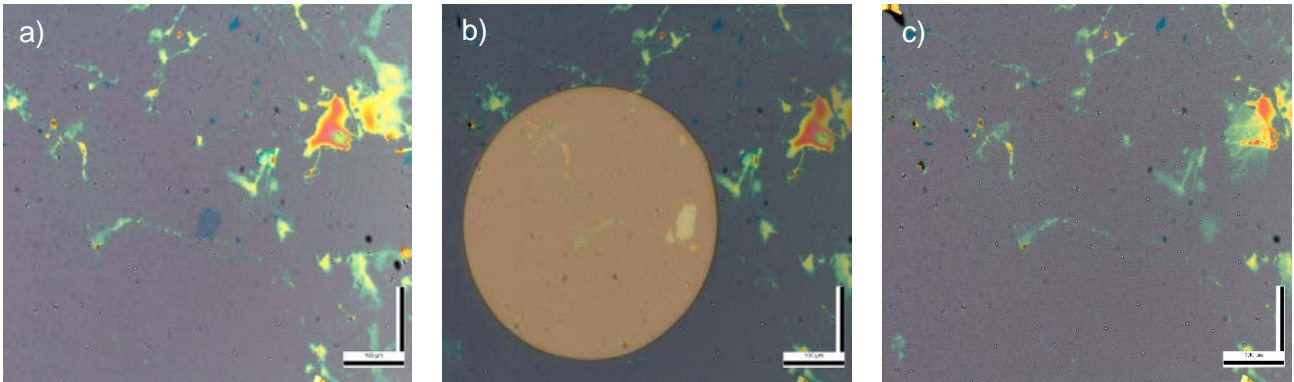


Figure 4.16: Optical image of a) graphene flake before final pickup, b) the twisted stamp containing hBN-gr in contact with the other half of gr and c) substrate after final pickup.

The half is brought in contact with hBN on stamp, heated up to  $\sim 55^{\circ}\text{C}$  and allowing ample time to slowly cool down to around  $\sim 40^{\circ}\text{C}$ . The stamp is later raised to pick up the gr attached to the hBN.

STEP 6: Controlled twist of the stage and pickup of the 2<sup>nd</sup> half of the graphene.

The stamp containing hBN and graphene is now brought over the 2<sup>nd</sup> half of the flake using the x-y stage control. The stage is now given the required twist and the stamp is brought in contact similar to step 5, as shown in Fig. 4.16.

STEP 7: hBN encapsulation to complete the stack.

The incomplete stack is brought in contact with one final hBN flake and the partial stack is dropped. Fig. 4.17 is a complete stack.

STEP 8: Analysis and post processing.

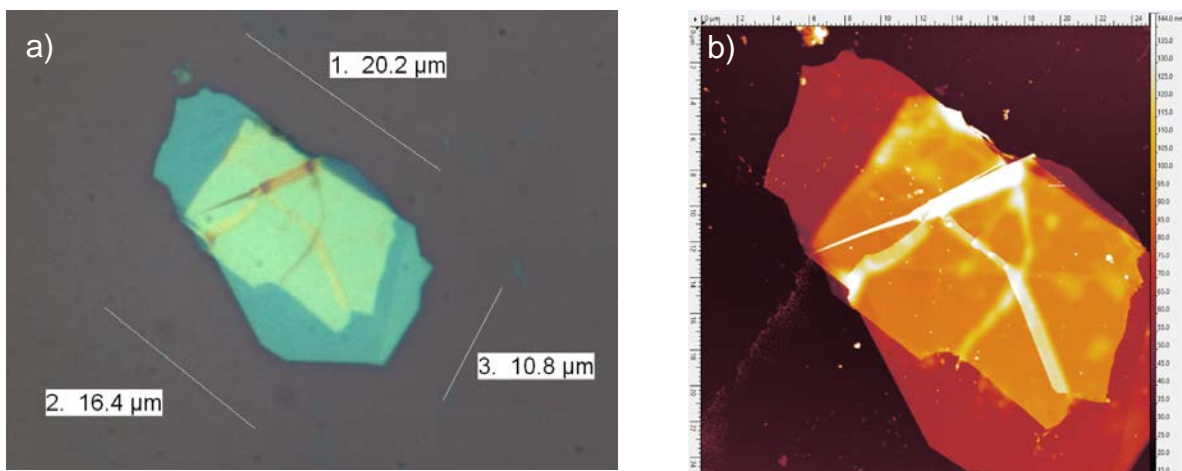


Figure 4.17: a) Optical Image of the final stack and b) AFM image of the same

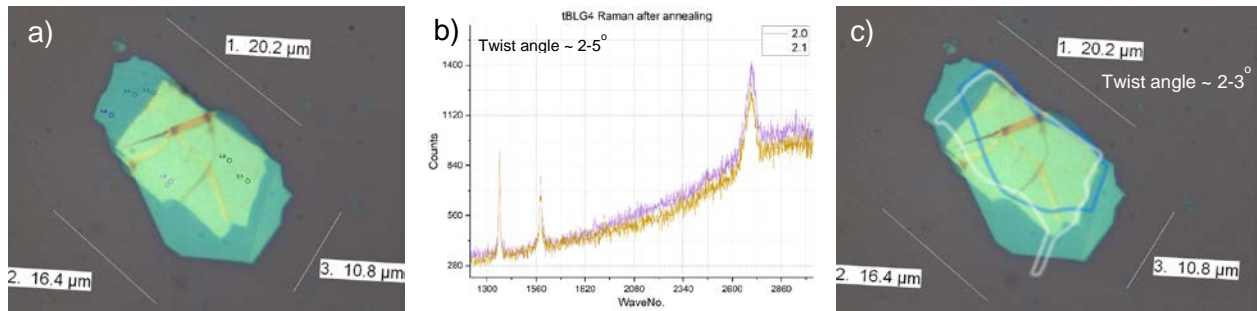


Figure 4.18: a) Stack with markings on Raman spectrum sites b) Relevant Raman Spectrum c) Optical Image with overlay of the gr flakes. The twist is estimated from the tear edges.

AFM in tapping mode is used to verify the overlapping bilayer region and mark bubble free regions. AFM Ironing may be used to significantly reduce the bubble in the region of interest. Raman Spectroscopy (for large angle tBLG) or optical image overlapping using some image manipulation tools like GIMP or Photoshop can lead to a rough determination of the twist angle.

For eg, in Fig. 4.18, Raman spectroscopy can be used to identify the large twist angle, in this case, it corresponds to that with a twist angle between 2-5°. While Optical image overlays suggest a twist angle between 2-3°.

#### 4.7 Future Prospects

- The procedure can be directly applied to fabricate Magic Angle tBLG as the major hinderances including tearing the graphene and maintaining a clean interface while stacking have been successfully explored and accounted for.
- Fabricating tBLG using different polymer material like PC (Polycarbonate) for stamp may be explored, since this is the most commonly used material in literature, although no distinct advantages have been found it is possible that PC (having a glass transition temperature ~ 55° C) is less likely to melt uncontrollably and hence a better candidate for the procedure.
- Since this is a generalised procedure, the same may be used to explore twistronics in other vdW heterostructures as well.

## 5. References

- [1] K. S. Novoselov, A. K. Geim, S. v. Morozov, D. Jiang, Y. Zhang, S. v. Dubonos, I. v. Grigorieva, and A. A. Firsov, *Electric Field in Atomically Thin Carbon Films*, *Science* (1979) **306**, 666 (2004).
- [2] C. Lee, X. Wei, J. W. Kysar, and J. Hone, *Measurement of the Elastic Properties and Intrinsic Strength of Monolayer Graphene*, *Science* (1979) **321**, 385 (2008).
- [3] E. Pop, V. Varshney, and A. K. Roy, *Thermal Properties of Graphene: Fundamentals and Applications*, *MRS Bull* **37**, 1273 (2012).
- [4] A. A. Balandin, S. Ghosh, W. Bao, I. Calizo, D. Teweldebrhan, F. Miao, and C. N. Lau, *Superior Thermal Conductivity of Single-Layer Graphene*, *Nano Lett* **8**, 902 (2008).
- [5] A. v. Rozhkov, G. Giavaras, Y. P. Bliokh, V. Freilikher, and F. Nori, *Electronic Properties of Mesoscopic Graphene Structures: Charge Confinement and Control of Spin and Charge Transport*, *Phys Rep* **503**, 77 (2011).
- [6] K. S. Novoselov, Z. Jiang, Y. Zhang, S. v. Morozov, H. L. Stormer, U. Zeitler, J. C. Maan, G. S. Boebinger, P. Kim, and A. K. Geim, *Room-Temperature Quantum Hall Effect in Graphene*, *Science* (1979) **315**, 1379 (2007).
- [7] H. B. Heersche, P. Jarillo-Herrero, J. B. Oostinga, L. M. K. Vandersypen, and A. F. Morpurgo, *Induced Superconductivity in Graphene*, *Solid State Commun* **143**, 72 (2007).
- [8] D. K. Efetov et al., *Specular Interband Andreev Reflections at van Der Waals Interfaces between Graphene and NbSe<sub>2</sub>*, *Nature Physics* 2015 12:4 **12**, 328 (2015).
- [9] J. O. Island et al., *Spin–Orbit-Driven Band Inversion in Bilayer Graphene by the van Der Waals Proximity Effect*, *Nature* 2019 571:7763 **571**, 85 (2019).
- [10] Z. Fei, W. Zhao, T. A. Palomaki, B. Sun, M. K. Miller, Z. Zhao, J. Yan, X. Xu, and D. H. Cobden, *Ferroelectric Switching of a Two-Dimensional Metal*, *Nature* 2018 560:7718 **560**, 336 (2018).
- [11] Z. Wang, I. Gutiérrez-Lezama, N. Ubrig, M. Kroner, M. Gibertini, T. Taniguchi, K. Watanabe, A. Imamoğlu, E. Giannini, and A. F. Morpurgo, *Very Large Tunneling Magnetoresistance in Layered Magnetic Semiconductor CrI<sub>3</sub>*, *Nature Communications* 2018 9:1 **9**, 1 (2018).
- [12] Y. Cao, V. Fatemi, S. Fang, K. Watanabe, T. Taniguchi, E. Kaxiras, and P. Jarillo-Herrero, *Unconventional Superconductivity in Magic-Angle Graphene Superlattices*, *Nature* 2018 556:7699 **556**, 43 (2018).

- 
- [13] Y. Cao et al., *Correlated Insulator Behaviour at Half-Filling in Magic-Angle Graphene Superlattices*, Nature 2018 556:7699 **556**, 80 (2018).
- [14] A. L. Sharpe, E. J. Fox, A. W. Barnard, J. Finney, K. Watanabe, T. Taniguchi, M. A. Kastner, and D. Goldhaber-Gordon, *Emergent Ferromagnetism near Three-Quarters Filling in Twisted Bilayer Graphene*, Science (1979) **365**, 605 (2019).
- [15] R. Bistritzer and A. H. Macdonald, *Moiré Bands in Twisted Double-Layer Graphene*, PNAS **108**, 12233 (2011).
- [16] E. Y. Andrei and A. H. MacDonald, *Graphene Bilayers with a Twist*, Nat Mater **19**, 1265 (2020).
- [17] C. W. J. Beenakker, *Colloquium: Andreev Reflection and Klein Tunneling in Graphene*, Rev Mod Phys **80**, 1337 (2008).
- [18] M. I. Katsnelson, K. S. Novoselov, and A. K. Geim, *Chiral Tunnelling and the Klein Paradox in Graphene*, Nature Physics 2006 2:9 **2**, 620 (2006).
- [19] R. Bistritzer and A. H. MacDonald, *Moiré Bands in Twisted Double-Layer Graphene*, Proc Natl Acad Sci U S A **108**, 12233 (2011).
- [20] C. Bena and G. M. Baux, *Remarks on the Tight-Binding Model of Graphene*, New J Phys **11**, 095003 (2009).
- [21] E. McCann and M. Koshino, *The Electronic Properties of Bilayer Graphene*, Reports on Progress in Physics **76**, 056503 (2013).
- [22] E. McCann and V. I. Fal'ko, *Landau-Level Degeneracy and Quantum Hall Effect in a Graphite Bilayer*, Phys Rev Lett **96**, 086805 (2006).
- [23] M. Koshino and T. Ando, *Orbital Diamagnetism in Multilayer Graphenes: Systematic Study with the Effective Mass Approximation*, Phys Rev B Condens Matter Mater Phys **76**, 085425 (2007).
- [24] A. Deshpande, W. Bao, Z. Zhao, C. N. Lau, and B. J. Leroy, *Mapping the Dirac Point in Gated Bilayer Graphene*, Appl Phys Lett **95**, 243502 (2009).
- [25] E. v. Castro, K. S. Novoselov, S. v. Morozov, N. M. R. Peres, J. M. B. L. dos Santos, J. Nilsson, F. Guinea, A. K. Geim, and A. H. C. Neto, *Biased Bilayer Graphene: Semiconductor with a Gap Tunable by the Electric Field Effect*, Phys Rev Lett **99**, 216802 (2007).
- [26] H. Min, B. Sahu, S. K. Banerjee, and A. H. MacDonald, *Ab Initio Theory of Gate Induced Gaps in Graphene Bilayers*, Phys Rev B Condens Matter Mater Phys **75**, 155115 (2007).
- [27] M. Yankowitz, J. Xue, D. Cormode, J. D. Sanchez-Yamagishi, K. Watanabe, T. Taniguchi, P. Jarillo-Herrero, P. Jacquod, and B. J. Leroy, *Emergence of Superlattice Dirac Points in Graphene on Hexagonal Boron Nitride*, Nature Physics 2012 8:5 **8**, 382 (2012).

- [28] H. Schmidt, T. Lüdtkke, P. Barthold, E. McCann, V. I. Fal'Ko, and R. J. Haug, *Tunable Graphene System with Two Decoupled Monolayers*, *Appl Phys Lett* **93**, 172108 (2008).
- [29] J. M. B. Lopes Dos Santos, N. M. R. Peres, and A. H. Castro Neto, *Graphene Bilayer with a Twist: Electronic Structure*, *Phys Rev Lett* **99**, 256802 (2007).
- [30] J. D. Sanchez-Yamagishi, T. Taychatanapat, K. Watanabe, T. Taniguchi, A. Yacoby, and P. Jarillo-Herrero, *Quantum Hall Effect, Screening, and Layer-Polarized Insulating States in Twisted Bilayer Graphene*, *Phys Rev Lett* **108**, 076601 (2012).
- [31] J. C. Slater and G. F. Koster, *Simplified LCAO Method for the Periodic Potential Problem*, *Physical Review* **94**, 1498 (1954).
- [32] G. Trambly De Laissardière, D. Mayou, and L. Magaud, *Numerical Studies of Confined States in Rotated Bilayers of Graphene*, *Phys Rev B Condens Matter Mater Phys* **86**, 125413 (2012).
- [33] Y. Cao, J. Y. Luo, V. Fatemi, S. Fang, J. D. Sanchez-Yamagishi, K. Watanabe, T. Taniguchi, E. Kaxiras, and P. Jarillo-Herrero, *Superlattice-Induced Insulating States and Valley-Protected Orbits in Twisted Bilayer Graphene*, *Phys Rev Lett* **117**, 116804 (2016).
- [34] K. Kim, A. DaSilva, S. Huang, B. Fallahazad, S. Larentis, T. Taniguchi, K. Watanabe, B. J. LeRoy, A. H. MacDonald, and E. Tutuc, *Tunable Moiré Bands and Strong Correlations in Small-Twist-Angle Bilayer Graphene*, *Proc Natl Acad Sci U S A* **114**, 3364 (2017).
- [35] A. K. Geim and I. v. Grigorieva, *Van Der Waals Heterostructures*, *Nature* 2013 499:7459 **499**, 419 (2013).
- [36] M. Yankowitz, Q. Ma, P. Jarillo-Herrero, and B. J. LeRoy, *Van Der Waals Heterostructures Combining Graphene and Hexagonal Boron Nitride*, *Nature Reviews Physics* 2018 1:2 **1**, 112 (2019).
- [37] A. K. Geim and K. S. Novoselov, *The Rise of Graphene*, *Nature Materials* 2007 6:3 **6**, 183 (2007).
- [38] TUINSTRAL F and KOENIG JL, *RAMAN SPECTRUM OF GRAPHITE*, *Journal of Chemical Physics* **53**, 1126 (1970).
- [39] Z. Ni, Y. Wang, T. Yu, and Z. Shen, *Raman Spectroscopy and Imaging of Graphene*, *Nano Res* **1**, 273 (2008).
- [40] A. C. Ferrari et al., *Raman Spectrum of Graphene and Graphene Layers*, *Phys Rev Lett* **97**, 187401 (2006).
- [41] Y. Zhang, Y. W. Tan, H. L. Stormer, and P. Kim, *Experimental Observation of the Quantum Hall Effect and Berry's Phase in Graphene*, *Nature* **438**, 201 (2005).

- 
- [42] X. Du, I. Skachko, A. Barker, and E. Y. Andrei, *Approaching Ballistic Transport in Suspended Graphene*, Nature Nanotechnology 2008 3:8 **3**, 491 (2008).
- [43] X. Du, I. Skachko, F. Duerr, A. Luican, and E. Y. Andrei, *Fractional Quantum Hall Effect and Insulating Phase of Dirac Electrons in Graphene*, Nature **462**, 192 (2009).
- [44] K. I. Bolotin, F. Ghahari, M. D. Shulman, H. L. Stormer, and P. Kim, *Observation of the Fractional Quantum Hall Effect in Graphene*, Nature 2009 462:7270 **462**, 196 (2009).
- [45] C. R. Dean et al., *Boron Nitride Substrates for High-Quality Graphene Electronics*, Nature Nanotechnology 2010 5:10 **5**, 722 (2010).
- [46] H. Li, X. Xiong, F. Hui, D. Yang, J. Jiang, W. Feng, J. Han, J. Duan, Z. Wang, and L. Sun, *Constructing van Der Waals Heterostructures by Dry-Transfer Assembly for Novel Optoelectronic Device*, Nanotechnology **33**, 465601 (2022).
- [47] S. G. Martanov, N. K. Zhurbina, M. v. Pugachev, A. I. Duleba, M. A. Akmaev, V. v. Belykh, and A. Y. Kuntsevich, *Making van Der Waals Heterostructures Assembly Accessible to Everyone*, Nanomaterials **10**, 1 (2020).
- [48] K. Kim et al., *Van Der Waals Heterostructures with High Accuracy Rotational Alignment*, Nano Lett **16**, 1989 (2016).
- [49] D. L. Mathieson, *The Tensile Strength of Paper*, Phys Teach **29**, 412 (1998).
- [50] K. Kim, S. Coh, L. Z. Tan, W. Regan, J. M. Yuk, E. Chatterjee, M. F. Crommie, M. L. Cohen, S. G. Louie, and A. Zettl, *Raman Spectroscopy Study of Rotated Double-Layer Graphene: Misorientation-Angle Dependence of Electronic Structure*, Phys Rev Lett **108**, (2012).
- [51] F. Pizzocchero, L. Gammelgaard, B. S. Jessen, J. M. Caridad, L. Wang, J. Hone, P. Bøggild, and T. J. Booth, *The Hot Pick-up Technique for Batch Assembly of van Der Waals Heterostructures*, Nat Commun **7**, (2016).
- [52] Y. Cao, V. Fatemi, S. Fang, K. Watanabe, T. Taniguchi, E. Kaxiras, and P. Jarillo-Herrero, *Unconventional Superconductivity in Magic-Angle Graphene Superlattices*, Nature 2018 556:7699 **556**, 43 (2018).